Article

Dopamine dynamics are dispensable for movement but promote reward responses

https://doi.org/10.1038/s41586-024-08038-z

Received: 21 July 2022

Accepted: 11 September 2024

Published online: 16 October 2024

Check for updates

Xintong Cai[1,6], Changliang Liu[1,6], Iku Tsutsui-Kimura[2], Joon-Hyuk Lee[1], Chong Guo[1], Aditi Banerjee[1], Jinoh Lee[1], Ryunosuke Amo[2], Yudi Xie[2], Tommaso Patriarchi[3,4], Yulong Li[5], Mitsuko Watabe-Uchida[2], Naoshige Uchida[2] & Pascal S. Kaeser[1]✉

Dopamine signalling modes differ in kinetics and spatial patterns of receptor activation[1,2]. How these modes contribute to motor function, motivation and learning has long been debated[3–21]. Here we show that action-potential-induced dopamine release is dispensable for movement initiation but supports reward-oriented behaviour. We generated mice with dopamine-neuron-specific knockout of the release site organizer protein RIM to disrupt action-potential-induced dopamine release. In these mice, rapid in vivo dopamine dynamics were strongly impaired, but baseline dopamine persisted and fully supported spontaneous movement. Conversely, reserpine-mediated dopamine depletion or blockade of dopamine receptors disrupted movement initiation. The dopamine precursor L-DOPA reversed reserpine-induced bradykinesia without restoring fast dopamine dynamics, a result that substantiated the conclusion that these dynamics are dispensable for movement initiation. In contrast to spontaneous movement, reward-oriented behaviour was impaired in dopamine-neuron-specific RIM knockout mice. In conditioned place preference and two-odour discrimination tasks, the mice effectively learned to distinguish the cues, which indicates that reward-based learning persists after RIM ablation. However, the performance vigour was reduced. During probabilistic cue-reward association, dopamine dynamics and conditioned responses assessed through anticipatory licking were disrupted. These results demonstrate that action-potential-induced dopamine release is dispensable for motor function and subsecond precision of movement initiation but promotes motivation and performance during reward-guided behaviours.

The striatum integrates input from midbrain dopamine neurons to control action and to facilitate learning. Phasic dopamine signalling relies on simultaneous firing of many dopamine neurons, synchronous release and coincident recruitment of dopamine receptors. Tonic signalling is mediated by stochastic receptor activations when firing is uncoordinated or absent[1,2]. The importance of the timing of dopamine regulation in these pathways remains debated. For example, previous studies have shown that rapid dopamine transients precede movement and are associated with movement initiation[3–6]. It is therefore implied that phasic dopamine triggers and modulates movement. Contrasting models of temporally precise dopamine action in movement, L-DOPA restores motor defects in patients with dopamine neuron loss in Parkinson's disease and in dopamine-depleted animals[14–17]. Dopamine signalling is also strongly associated with learning and motivation, with proposed roles for both slow and fast mechanisms[7,9,20,21]. In learning, the importance of rapid dopamine action is rooted in the observations that phasic dopamine has reinforcing effects and that it resembles the reward prediction error term in reinforcement learning theories[9–13], although these models remain contested[18,19]. Altogether, these and other studies have provided approaches and models on the function of dopamine in the moment-to-moment regulation of action[22–29]. However, it has remained uncertain whether rapid dopamine transients are necessary for movement control, motivation and learning.

Movement without induced dopamine release

Phasic dopamine release underlies rapid dopamine dynamics measured in vivo[1,30–32]. To disrupt these dynamics, we removed the release site organizer RIM, a protein important for action-potential-induced dopamine exocytosis, by crossing conditional RIM1 and RIM2 knockout mice to *Dat*$^{Ires\text{-}cre}$ mice (hereafter termed RIM cKO^{DA} mice). In acute brain slices, electrically induced dopamine release is mediated by action potentials (Extended Data Fig. 1a–c) and is severely impaired in these mice when assessed using amperometry or electrophysiology[33–36]. We first confirmed that release was disrupted across dorsal striatal areas.

[1]Department of Neurobiology, Harvard Medical School, Boston, MA, USA. [2]Department of Molecular and Cellular Biology, Center for Brain Science, Harvard University, Cambridge, MA, USA. [3]Institute of Pharmacology and Toxicology, University of Zurich, Zurich, Switzerland. [4]Neuroscience Center Zurich, ETH and University of Zurich, Zurich, Switzerland. [5]State Key Laboratory of Membrane Biology, Peking University School of Life Sciences, Beijing, China. [6]These authors contributed equally: Xintong Cai, Changliang Liu. ✉e-mail: kaeser@hms.harvard.edu

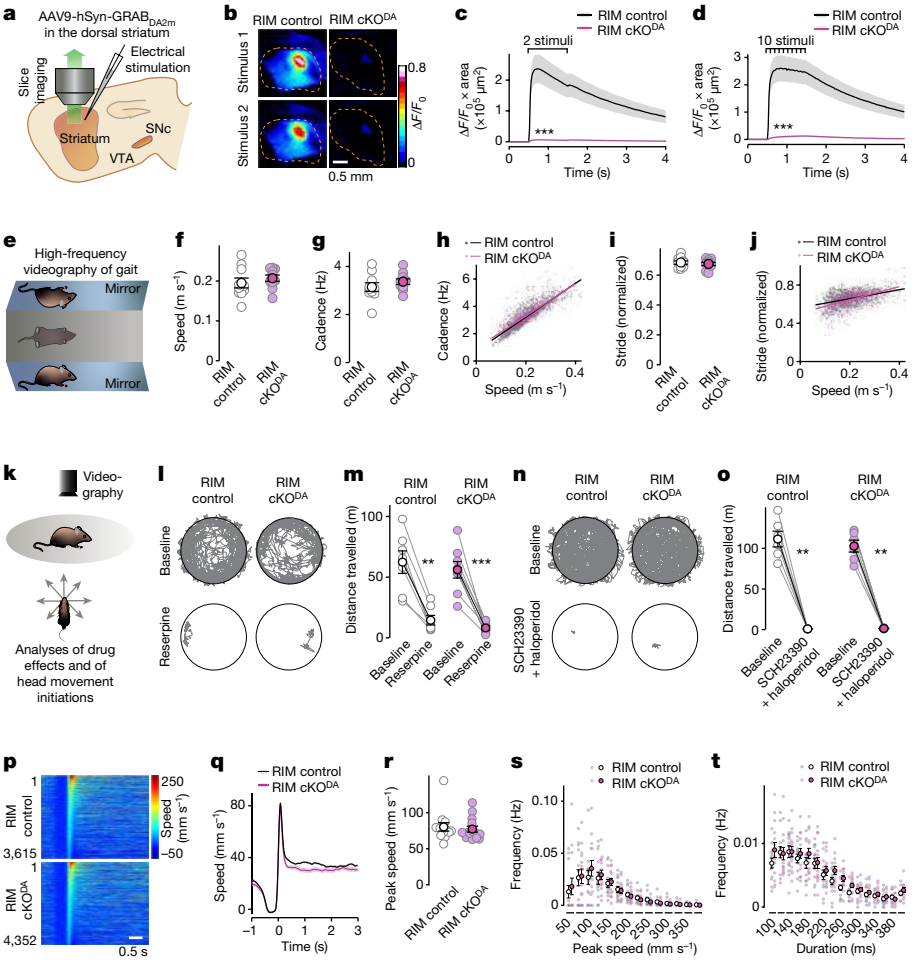

Fig. 1 | Normal motor function after disrupting induced dopamine release. **a**, Schematic of imaging in parasagittal slices of RIM cKO^{DA} mice and RIM control mice[33]. SNc, substantia nigra pars compacta; VTA, ventral tegmental area. **b**–**d**, Representative images (**b**) and quantification (**c**,**d**) of dopamine release monitored by GRAB$_{DA}$ fluorescence (dashed lines outline the striatum), induced by paired (1 Hz; **b**,**c**) or 10 stimuli (10 Hz; **d**). RIM control, 8 slices from 3 mice; RIM cKO^{DA}, 11 slices from 3 mice. **e**, Schematic of gait analyses. **f**–**h**, Average speed (**f**) and cadence (**g**) across gait cycles, and scatter plot and linear regression thereof (**h**). RIM control, $R = 0.88$ in 1,122 cycles from 10 mice; RIM cKO^{DA}, $R = 0.85$ in 1,206 cycles from 10 mice. **i**,**j**, As **f**–**h**, but for stride length against speed, RIM control $R = 0.42$ in 1,122 cycles from 10 mice, RIM cKO^{DA} $R = 0.57$ in 1,206 cycles from 10 mice. **k**, Schematic of movement initiation analyses of drug effects (**l**–**o**) and head movement initiations (**p**–**t**) in a round arena. **l**,**m**, Representative trajectories (**l**) and quantification of distance travelled in 30 min (**m**) before and after i.p. injection of reserpine (2 mg kg^{-1}). RIM control, 7 mice; RIM cKO^{DA}, 8 mice. **n**,**o**, As for **l**,**m**, but for i.p. injection of D_1 (SCH23390, 1 mg kg^{-1}) and D_2 (haloperidol, 2 mg kg^{-1}) receptor antagonists. RIM control, 6 mice; RIM cKO^{DA}, 6 mice. **p**–**r**, Individual (**p**) and average time courses (**q**) of movement initiations, and peak speed per mouse (**r**). Event heatmaps (**p**) were sorted by the peak speed amplitude. RIM control, 3,615 events from 13 mice; RIM cKO^{DA}, 4,352 events from 14 mice. **s**,**t**, Frequency of peak speeds (**s**) and durations (**t**) of detected movement events above the indicated cut-off values, numbers of events and mice as in **p**–**r**. Data are the mean ± s.e.m. $^{**}P < 0.01$, $^{***}P < 0.001$ as assessed by two-sided Mann–Whitney rank-sum tests (**c**,**d**,**f**,**g**,**i**,**m**,**o**,**q**,**r**) or two-way analysis of variance (ANOVA) (**s**,**t**). For dopamine amperometry and additional analyses of motor function, see Extended Data Fig. 1. Exact *P* values for this and all subsequent figures are in Supplementary Table 1.

After RIM ablation, induced dopamine release was strongly impaired throughout the dorsal striatum when assessed in brain slices with the D_2 receptor-based fluorescent dopamine sensor GRAB$_{DA2m}$ (abbreviated as GRAB$_{DA}$)[30,31] (Fig. 1a–d) and when tested at multiple locations using amperometry[33,34] (Extended Data Fig. 1d–i). In contrast to studies that removed NMDA receptors from dopamine neurons[37,38], we here disrupted dopamine release in response to both pacemaker and burst firing, and most of the persisting extracellular dopamine was independent of action potentials[33–35,39,40].

Notably, no impairments in basic motor functions were detected in RIM cKO^{DA} mice. We first evaluated the subsecond structure of gait. In high-frequency videos of mice walking on a linear path, the nose, paws, rear-end and tail tip were tracked using a convolutional neural network (Supplementary Video 1). Individual gait cycles were segregated using a hidden Markov model and analysed. The structure of gait was indistinguishable between RIM control mice and RIM cKO^{DA} mice (Fig. 1e–j and Extended Data Fig. 1j–t). Correspondingly, no differences were detected in bar crossing and climbing tests and in rotarod tests (Extended Data Fig. 1u–z).

Despite the strong reduction in induced dopamine release in brain slices, basal extracellular dopamine levels measured using microdialysis persisted in RIM cKO^{DA} mice and amounted to about 30% of those in control mice[33,34]. Similar basal dopamine levels are detected in mice without genetic disruption of the release machinery after local blockade of action potential firing[33,34,41]. To test whether this action-potential-independent dopamine release contributes to spontaneous movement, we tracked mouse movement before and after depletion of brain dopamine with the vesicular monoamine transporter blocker reserpine. We also assessed movement before and after inhibition of dopamine signalling with D_1 (SCH23390) and D_2 (haloperidol) receptor blockers. Intraperitoneal (i.p.) injection of these drugs induced bradykinesia in both RIM control mice and

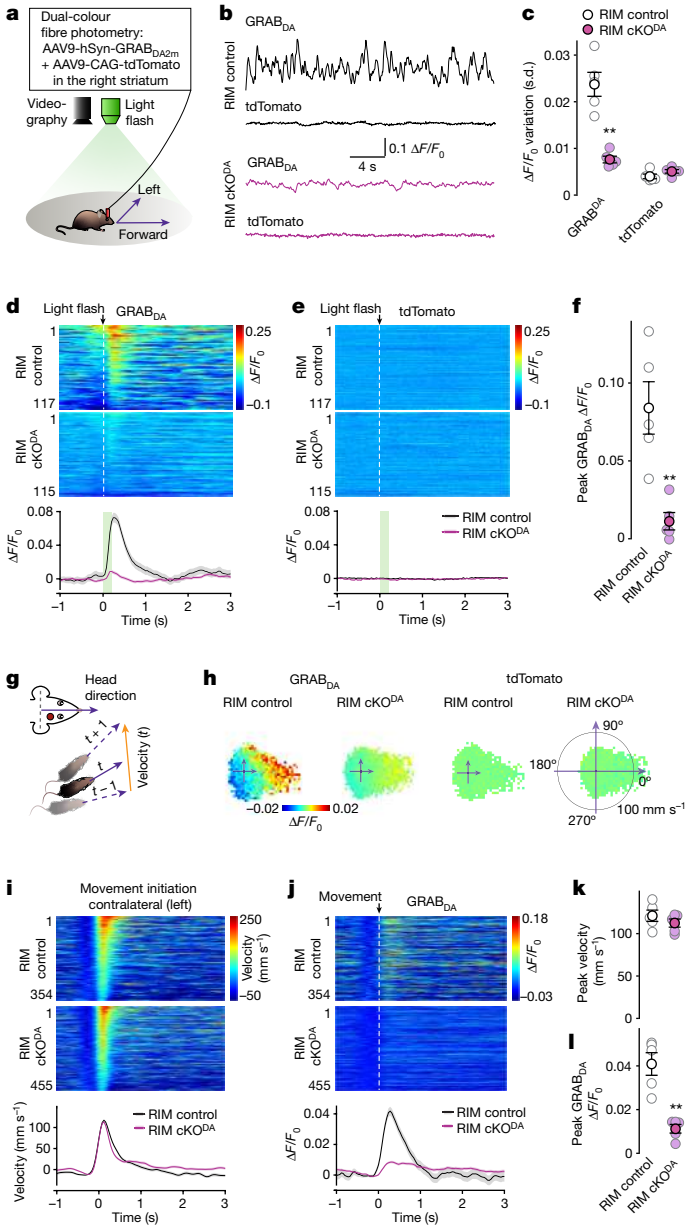

Fig. 2 | Disrupted in vivo dopamine dynamics but unaltered movement initiation in RIM cKO^{DA} mice. a, Schematic of the experiment. The fibre photometric canula was in the right dorsal striatum. **b**,**c**, Example traces (**b**) and quantification (**c**) of fluorescence variation quantified as the s.d. of $\Delta F/F_0$ of GRAB$_{DA}$ and tdTomato fluorescence. RIM control, 5 mice; RIM cKO^{DA}, 5 mice. **d**–**f**, Time course of fluorescence in individual trials (event heatmaps, top) and average data (bottom) for GRAB$_{DA}$ (**d**) and tdTomato (**e**) fluorescence aligned to the sensory stimulation (dashed line), and peak GRAB$_{DA}$ per mouse (**f**). Event heatmaps in **d**,**e** were sorted by the peak amplitude in **d**. RIM control, 117 events from 5 mice; RIM cKO^{DA}, 115 events from 5 mice. **g**, Schematic of movement initiation analyses as previously established[30]. **h**, Average GRAB$_{DA}$ and tdTomato signals registered to their concurrent velocity. Each velocity vector was plotted in polar coordinates, and the corresponding fluorescence changes ($\Delta F/F_0$) were mapped onto these velocity vectors for each genotype and fluorophore. **i**–**l**, Individual (event heatmaps, top) and average (bottom) time courses of velocity amplitudes (**i**) and GRAB$_{DA}$ fluorescence changes (**j**) during contralateral movement initiations (left turns, velocity angles between 0° and 180°), and peak velocity (**k**) and GRAB$_{DA}$ (**l**) per mouse. Event heatmaps in **i**,**j** were sorted by the peak velocity amplitude. RIM control, 354 events from 5 mice; RIM cKO^{DA}, 455 events from 5 mice. Data are the mean ± s.e.m. $^{**}P < 0.01$, assessed by two-sided Mann–Whitney rank-sum test (**c**,**f**,**k**,**l**). See Extended Data Figs. 2–5 for assessment of locomotion after dopamine receptor blockade, $\Delta F/F_0$ variation as a function of excitation power output, $\Delta F/F_0$ variation after sodium channel blockade, $\Delta F/F_0$ variation before and after GRAB$_{DA}$ blockade, additional movement-related GRAB$_{DA}$ fluorescence of RIM cKO^{DA} mice, dopamine axon Ca^{2+} dynamics with GCaMP6s of RIM cKO^{DA} mice, and dopamine release with RdLight1.

RIM cKO^{DA} mice (Fig. 1k–o and Extended Data Fig. 1aa,ab), thereby establishing that dopamine signalling remains crucial for spontaneous movement after RIM ablation. We next performed unilateral dopamine axon lesions with 6-hydroxydopamine (6-OHDA) and induced rotations using the dopamine receptor agonist apomorphine[42]. Overall, rotations were similar in RIM control mice and RIM cKO^{DA} mice (Extended Data Fig. 1ac,ad). This result suggests that dopamine receptor super-sensitivity, induced by dopamine denervation[42], is similar in RIM cKO^{DA} mice and control mice and not occluded in the mutant mice.

We next extracted movement initiations of mice in an open-field arena (Fig. 1k,p–t and Extended Data Fig. 1ae,af). We assessed the peak head speed and the duration of movement events in all directions (Fig. 1p–r) and calculated how frequent specific speeds and durations occurred (Fig. 1s,t). Overall, these parameters were highly similar between RIM control mice and RIM cKO^{DA} mice. We conclude that spontaneous movement initiation depends on dopamine signalling, but action-potential-induced dopamine release seems to be dispensable. These findings complement previous work showing that dopamine-depleted animals can initiate movement in the presence of strong external stimuli[43].

Disrupted dopamine dynamics without RIM

To directly test the relationship between rapid dopamine signals and movement, we monitored dopamine dynamics in the dorsal striatum using fibre photometry with GRAB$_{DA}$ in mice moving in an open-field arena (Fig. 2a; the cannula was targeted to the medial area of the dorsolateral striatum)[30]. Local infusion of dopamine receptor blockers to inhibit dopamine signalling in the imaging area substantially reduced movement (Extended Data Fig. 2a–c). Dopamine fluctuations, measured as the variation of GRAB$_{DA}$ fluorescence ($\Delta F/F_0$), were strongly reduced in RIM cKO^{DA} mice (Fig. 2b,c and Extended Data Figs. 2 and 3). To assess induced dopamine transients in vivo, we used sensory stimulation with 200-ms-long illuminations of the open field (50 µW cm^{-2}) at random intervals while the mice explored the arena (Fig. 2d–f). We detected phase-locked dopamine transients in RIM control mice and an approximately 90% decrease in RIM cKO^{DA} mice. These findings are similar to results from slice experiments[33,34] (Fig. 1a–d and Extended Data Fig. 1a–i) and establish that rapid dopamine dynamics are disrupted in vivo after ablating RIM from dopamine neurons.

Rapid dopamine transients have been proposed to trigger movement[3,4]. To assess the relationship between fast dopamine dynamics and movement initiation, velocity was defined as a two-dimensional vector relative to head direction (Fig. 2g). Meanwhile, fluorescence changes in photometry were registered to their corresponding velocities in polar coordinate plots[30]. In RIM control mice, dopamine levels were highly related to movement direction (Fig. 2h and Extended Data Fig. 3d). In RIM cKO^{DA} mice, changes in GRAB$_{DA}$ fluorescence were strongly reduced. We subgrouped movement initiations into contralateral turns relative to the fibre photometric canula (in the right striatum, left turns with a velocity angle between 0° and 180°) and ipsilateral turns (right turns with a velocity angle between 180° and 360°) and aligned the measured dopamine transients to them. The velocity amplitude and time course of these turns were similar between RIM cKO^{DA} mice and control mice (Fig. 2i,k). In RIM control mice, dopamine transients exhibited an increase or a decrease during contralateral or ipsilateral turns, respectively (Fig. 2j,l and Extended Data Fig. 3e–i). These transients were substantially impaired in RIM cKO^{DA} mice. In conclusion, fast

dopamine transients are strongly correlated with movement initiations, a finding similar to previous work[3–6,30]. However, these rapid dynamics can be disrupted without effects on movement initiation and on its kinetic features (Fig. 2g–l). Moreover, the time course of dopamine transients compared to turning velocity was delayed[30] (Extended Data Fig. 3d). Together, these results indicate that it is unlikely that dopamine triggers movement.

Similar methods were used to assess Ca^{2+} fluctuations in dopamine axons with GCaMP6s and striatal dopamine changes with RdLight1, a red-shifted, D_1 receptor-based dopamine sensor[32] (Extended Data Figs. 4 and 5). Overall, axonal Ca^{2+} fluctuations were similar between the mouse genotypes, whereas dopamine transients monitored with this alternative sensor were disrupted after RIM ablation. These data indicate that this impairment in dopamine dynamics is unlikely due to a loss of dopamine neuron firing.

L-DOPA does not restore dopamine dynamics

The results from RIM cKO^{DA} mice establish that most dopamine dynamics are dispensable for subsecond control of spontaneous movement when dopamine release is disrupted through RIM ablation throughout development. In search of an alternative approach, we also tested mice with synaptotagmin-1 ablated from dopamine neurons (Syt-1 cKO^{DA} mice), which abolishes synchronous dopamine release in brain slices[41]. In vivo, however, the remaining release, presumably asynchronous release[41,44], maintains dopamine dynamics in these mice; therefore, Syt-1 cKO^{DA} mice are not suited to test roles of these dynamics in behaviour (Extended Data Fig. 6).

We next used pharmacological manipulations to acutely disrupt dopamine release, effectively preventing putative compensation that might be present in genetic experiments. Foundational work revealed that the dopamine precursor L-DOPA restores movement after dopamine depletion with the vesicular monoamine transporter blocker reserpine[16,17]. For the treatment of Parkinson's disease, the leading model is that L-DOPA promotes movement through constant dopamine receptor stimulation[14]. It is unclear whether L-DOPA restores some fast dopamine dynamics, and how it might lead to constant receptor activation remains uncertain. We tested whether L-DOPA promotes movement without restoring dopamine dynamics.

We used intraperitoneal (i.p.) reserpine injection to deplete dopamine, which induced bradykinesia and eliminated striatal dopamine fluctuations (Fig. 3a–e). Subsequent L-DOPA i.p. injection restored movement and enhanced baseline dopamine, but failed to re-establish dopamine dynamics (Fig. 3b–e and Extended Data Fig. 7). Brief illuminations of the arena did not elicit dopamine responses in these mice, thereby establishing that induced dopamine release was disrupted (Extended Data Fig. 8). Although the turning velocity was restored to pre-reserpine levels after L-DOPA injection, turning-associated dopamine transients were strongly impaired in the polar coordinate plots and were undetectable in isolated left turns (Fig. 3f–j and Extended Data Fig. 9a–e).

To examine whether RIM ablation or dopamine depletion followed by L-DOPA left behind a small amount of rapid dopamine sufficient to trigger movement, we combined these manipulations (Fig. 3k–n and Extended Data Fig. 9f–j). Movement in RIM cKO^{DA} mice was sensitive to reserpine depletion, and resupplying L-DOPA restored movement initiation. The small $GRAB_{DA}$ fluorescence increase detected in RIM cKO^{DA} mice at movement onset was abolished by reserpine and by treatment with reserpine plus L-DOPA. These data indicate that it is highly unlikely that a small amount of phasic dopamine in RIM cKO^{DA} mice or after reserpine plus L-DOPA treatment triggers movement initiation. Altogether, movement initiation was intact even when dopamine dynamics were ablated post-developmentally within a 24 h time window. Our data establish that L-DOPA ameliorates movement without enhancing rapid dopamine dynamics.

Impaired performance vigour without RIM

We next tested whether action-potential-induced dopamine release is necessary for reward-oriented behaviour and learning. We first assessed RIM cKO^{DA} mice in food-associated conditioned place preference (food-CPP), a task that tests for reinforcing effects of food, including the motivation for reward[45]. RIM cKO^{DA} mice formed food-CPP similar to controls, but they entered the centre area less often, which suggested that they are less motivated to seek food (Fig. 4a–e). These results indicate that the ability to associate a food stimulus with environmental context is intact in RIM cKO^{DA} mice. However, the motivation to seek food seemed reduced, which was in contrast to the unaltered level of general exploration of an open arena (Fig. 1k–o).

Next, to assess the vigour of reward-oriented movement, we trained RIM cKO^{DA} mice and RIM control mice in an odour-guided perceptual decision-making task[46]. Mice initiated a trial with a nose poke in a central port, which in turn provided an odour that indicated the side port at which a water reward will be delivered (Fig. 4f). RIM cKO^{DA} mice initiated fewer trials and took longer before initiating the next trial independent of whether the preceding trial was a success (reward obtained) or a failure (no reward) than RIM control mice. However, both RIM control mice and RIM cKO^{DA} mice learned the task (Fig. 4g–j). Despite accurate task execution and unaltered reaction time after presentation of the odour, RIM cKO^{DA} mice moved slower from the odour port to the water port and consequently took more time to complete a single trial (Fig. 4k–m). Together, these results indicate that action-potential-induced dopamine release is not needed for the process of reinforcement learning in these two tasks. By contrast, it refines reward-oriented movement as its disruption affects rapid and consistent performance.

Conditioned behaviour without RIM

Dopamine dynamics resemble a teaching signal that encodes the discrepancy between expected and obtained reward[9–13]. To test the roles of this reward prediction error-related dopamine signal, we adapted a probabilistic conditioning task[12] during which we evaluated dopamine dynamics in head-fixed RIM cKO^{DA} mice and RIM control mice. This task has been used to assess these dopamine signals. It can further serve to test whether dopamine supports motivation to participate in the task, promotes learning to predict reward probability and facilitates expression of learning through anticipatory behaviour. Induced dopamine release is disrupted in the ventral striatum of RIM cKO^{DA} mice when assessed using amperometry in brain slices[33]. Correspondingly, $GRAB_{DA}$ transients in brain slices and dopamine fluctuations in vivo were strongly reduced in the ventral striatum after RIM ablation (Extended Data Fig. 10a–h).

The mice were trained on 20 consecutive days to predict the probabilities of water rewards in response to three specific odours, and dopamine dynamics were monitored by fibre photometry (Fig. 5a and Extended Data Fig. 10i,j). The head-fixed mice collected the water reward by licking at reward delivery. Anticipatory licking between odour and reward delivery was quantified as a learned behaviour during this task. Free water trials in which an unexpected reward was delivered were intermixed.

In free water trials, reward consumption of RIM control mice was accompanied by increasing dopamine responses over the 20-day training period (Fig. 5b–e and Extended Data Fig. 10r,s). On day 1 of training, RIM cKO^{DA} mice effectively consumed free rewards with a normal peak lick frequency. However, late in the training, RIM control mice showed an increase in sustained licking after free water delivery (Fig. 5e and Extended Data Fig. 10r,s), whereas RIM cKO^{DA} mice did not increase this behavioural response, which possibly reflects decreased motivation. Dopamine transients were strongly impaired, and reward consumption failed to boost dopamine responses over time in RIM cKO^{DA} mice. The correlation between defects in sustained licking and

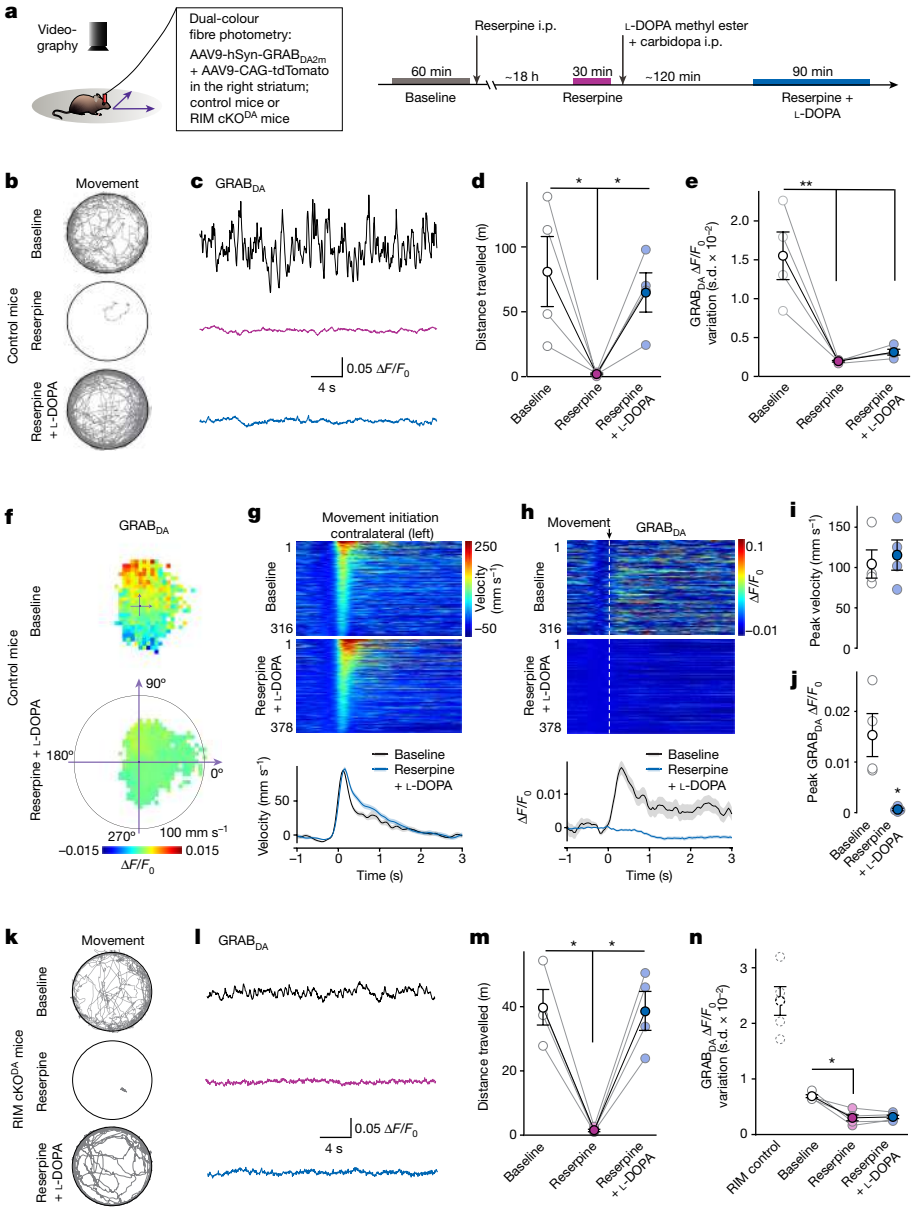

Fig. 3 | L-DOPA restores movement but not dopamine dynamics. a, Schematic of the experiment and of the time course of drug treatment (i.p. dosage: 3 mg kg^{-1} reserpine, 250 mg kg^{-1} L-DOPA methyl ester, 25 mg kg^{-1} carbidopa) of control mice (**b**–**j**) and RIM cKO^{DA} mice (**k**–**n**). **b**–**e**, Representative traces of trajectories (**b**) and GRAB$_{DA}$ signals (**c**), and quantification of distance travelled over 30 min (**d**) and GRAB$_{DA}$ variation (**e**) in mice in an open field. Control, 4 mice. **f**–**j**, Average GRAB$_{DA}$ signals registered to concurrent velocity in polar coordinates (**f**), individual (event heatmaps, top) and average (bottom) time course of velocity amplitudes (**g**) and GRAB$_{DA}$ fluorescence changes (**h**) during contralateral movement initiations (left turns, velocity angles between 0° and 180°), and peak velocity (**i**) and GRAB$_{DA}$ (**j**) per mouse. Event heatmaps in **g**,**h** were sorted by the peak velocity amplitude. Baseline, 316 events from 4 mice; reserpine plus L-DOPA, 378 events from 4 mice. **k**–**n**, As for **b**–**e**, but for RIM cKO^{DA} mice. In **n**, the RIM control condition is replotted from Fig. 2c for comparison. RIM cKO^{DA}, 4 mice. Data are the mean ± s.e.m. *P < 0.05, **P < 0.01, assessed by Kruskal–Wallis ANOVA with post hoc Dunn's tests (**d**,**e**,**m**,**n** (vs reserpine)) or two-sided Mann–Whitney rank-sum tests (**i**,**j**). See Extended Data Figs. 6–9 for assessment of Syt-1 cKO^{DA} mice, F_0 and movement after reserpine plus L-DOPA, additional GRAB$_{DA}$ fluorescence in control and reserpinized mice, and additional GRAB$_{DA}$ fluorescence in RIM cKO^{DA} mice.

in dopamine signals suggests that dopamine magnifies the behavioural response to reward.

In odour trials, the mice were trained to associate odours with rewards with a specific probability: 80% reward for odour 1 (100% in the initial training phase from days 1–7); 40% reward for odour 2; and no reward for odour 3. RIM control mice strongly increased anticipatory licking over time in proportion to reward probability (Fig. 5f and Extended Data Fig. 10k). By contrast, RIM cKO^{DA} mice showed substantially reduced anticipatory licking in response to odours associated with 80% and 40% reward probabilities (Fig. 5f). Nevertheless, the mice effectively collected rewards (Fig. 5g), similar to the free water trials.

Analyses of dopamine responses in the ventral striatum on day 17 (Fig. 5h–l) revealed reward prediction error-like dopamine signals in RIM control mice. There were large dopamine transients in response to odours 1 and 2. At reward delivery, there was either a reward-associated dopamine signal (in rewarded trials) or a dip (in omission trials). In RIM cKO^{DA} mice, the magnitude of dopamine dynamics was substantially decreased.

Altogether, these results establish a central role for RIM-dependent dopamine dynamics in this probabilistic cue-reward association task. In RIM cKO^{DA} mice, dopamine responses to reward and to reward-predicting cues are disrupted. Although these mice can in principle

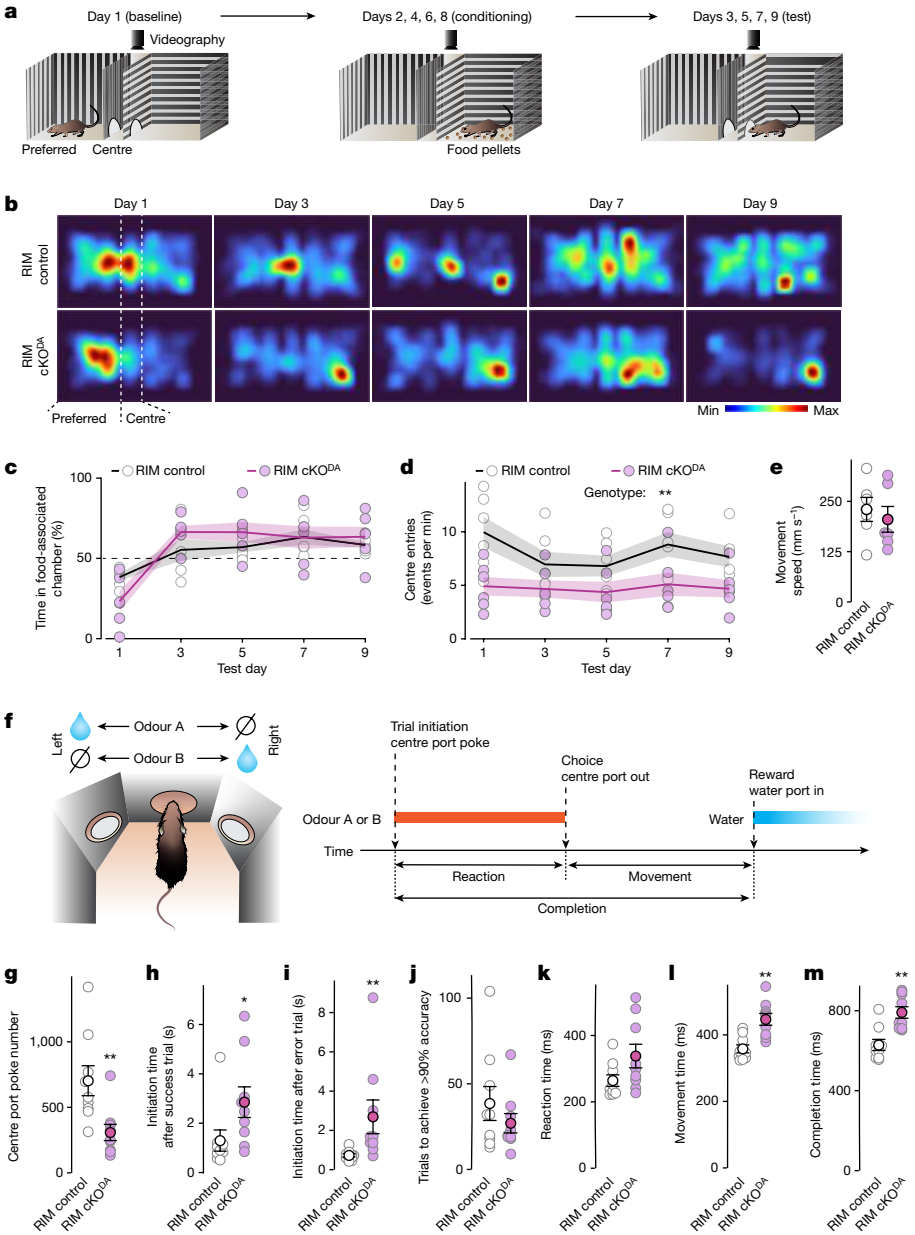

Fig. 4 | RIM cKO^{DA} mice learn to make binary choices but the vigour of reward-oriented behaviour is reduced. a, Schematic of food-CPP in which the less preferred side at baseline (day 1) is associated with food on days 2, 4, 6 and 8. On days 3, 5, 7 and 9, place preference was assessed. **b**–**e**, Representative example heatmaps of mouse location in the CPP arena (**b**) and quantification of the percentage of time spent on test days in the food-associated chamber (**c**), of frequency of entries into the centre of the CPP apparatus (**d**) and of movement speed during these centre entries (**e**). In the heatmaps (**b**), the time spent of each mouse is normalized in each session. RIM control, 6 mice; RIM cKO^{DA}, 6 mice. **f**, Schematic and time course of the perceptual decision-making task in which the correct choice after exposure to odour A or B is rewarded by a water drop. The data were collected while mice learned to discriminate two odours. **g**–**j**, Quantification of the number of centre port pokes (**g**), trial initiation times (**h**,**i**) and the number of trials it took to achieve >90% accuracy for two consecutive sessions (**j**) over all trials. RIM control, 9 mice; RIM cKO^{DA}, 9 mice. **k**–**m**, Quantification of the reaction time (**k**), movement time (**l**) and trial completion time (**m**) in the first two sessions. Times were calculated as the median of all trials for each mouse. Number of mice as in **g**–**j**. Data are the mean ± s.e.m. $^{*}P < 0.05$, $^{**}P < 0.01$, assessed by two-way ANOVA (**c**,**d**) or two-sided Mann–Whitney rank-sum tests (**e**,**g**–**m**).

learn to make reward-based decisions, conditioned behavioural responses are impaired.

Discussion

Correlative studies are often used to develop models on how neural activity controls behaviour. In the case of dopamine, it has remained difficult to move from correlation to causation. A key challenge has been to mechanistically define the different dopamine signalling modes and to determine their functions[1,2,7]. We here adapted approaches to assess roles of rapid dopamine dynamics in movement, motivation and learning by disrupting action-potential-induced dopamine release (Supplementary Discussion). We show that the remaining stochastic dopamine signalling is sufficient to drive movement with subsecond precision. By contrast, although mice with disrupted dopamine dynamics can learn to make reward-based decisions, they have strongly impaired behavioural responses to anticipated rewards. We conclude that rapid dopamine dynamics are dispensable for movement initiation but the role of RIM in action-potential-mediated dopamine release is important for reward-guided conditioned behaviours.

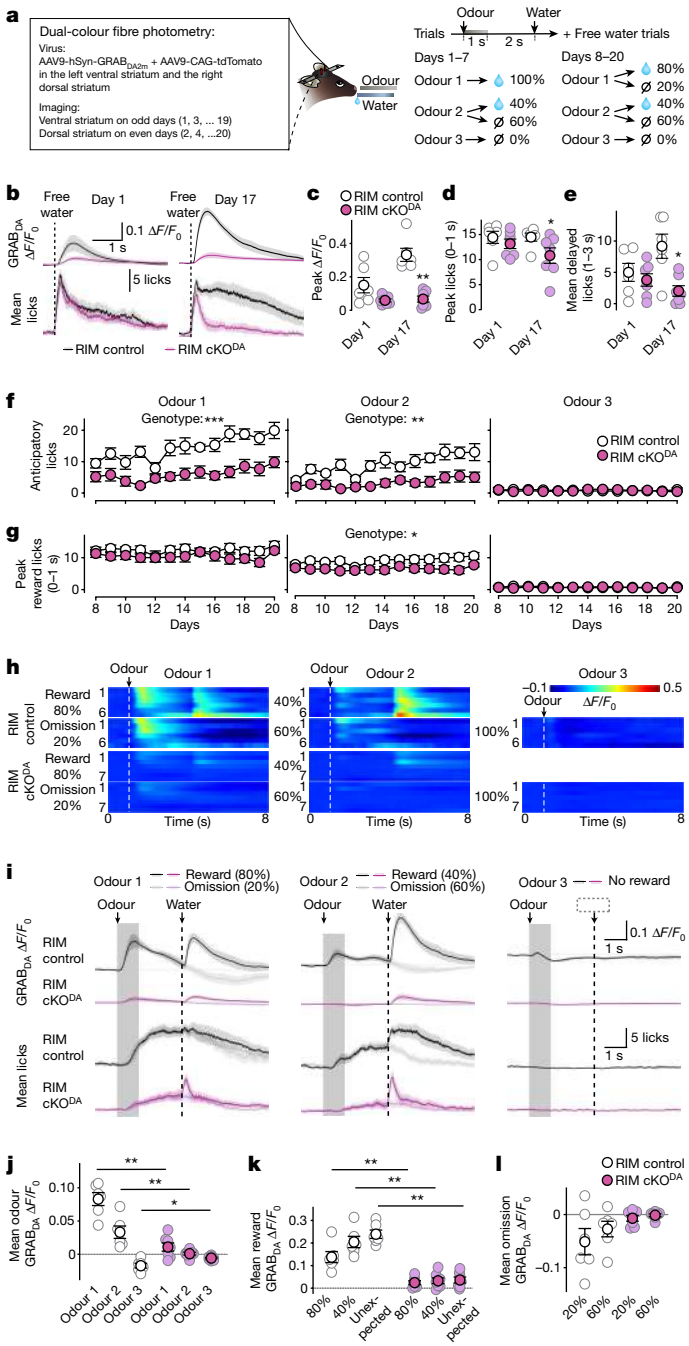

Fig. 5 | Disrupted anticipatory behaviour of RIM cKO^{DA} mice in a probabilistic cue-reward association task. a, Schematic of the task in head-fixed mice. **b**–**e**, Quantification of free water trials with the time course of GRAB$_{DA}$ fluorescence (**b**, top) and licking (**b**, bottom) aligned to free water delivery (dashed line) on days 1 and 17 of the training (**b**), and peak GRBA$_{DA}$ (**c**), peak licks (**d**) and mean delayed licks (**e**). RIM control, 6 mice; RIM cKO^{DA}, 7 mice. **f**,**g**, Quantification of odour trials with anticipatory licks during the 2-s time window between odour and water delivery (**f**) and peak licks to reward within the first second of water delivery (**g**) for odour 1 (80% reward), odour 2 (40% reward) and odour 3 (no reward) from day 8 to day 20. Numbers of mice as in **b**–**e**. **h**,**i**, Quantification of odour trials with time course of GRAB$_{DA}$ fluorescence (**h**, heatmaps), average GRAB$_{DA}$ fluorescence (**i**, top) and licking (**i**, bottom) aligned to odour and water delivery per mouse. Heatmaps in **h** are sorted by the peak amplitude in odour 1 for each genotype. Numbers of mice as in **b**–**e**. **j**–**l**, Average GRAB$_{DA}$ for each odour (**j**, within 3 s from odour onset) and average GRAB$_{DA}$ for reward trials (**k**, within 201–1,200 ms from water onset) and omission trials (**l**, within 1,501–2,500 ms from water onset). Numbers of mice as in **b**–**e**. Data are the mean ± s.e.m. $^*P < 0.05$, $^{**}P < 0.01$, $^{***}P < 0.001$ assessed by two-sided Mann–Whitney rank-sum tests (**c**,**d**,**e**,**j**–**l**) or two-way ANOVA (**f**,**g**). See Extended Data Fig. 10 for additional assessment of licking and of GRAB$_{DA}$ fluorescence in slices and in vivo. See Supplementary Figs. 1–4 for analyses of licking and dopamine dynamics on each training day.

The mechanisms and roles of action-potential-independent dopamine signalling are unclear. This form of release might contribute to functions of tonic dopamine[1,7,9,21], but the underlying mechanisms remain poorly defined. Because most dopamine release is vesicular, spontaneous release generates small-scale, high-concentration dopamine sparks that act on nearby receptors rather than homogenous low levels of extracellular dopamine to evenly and persistently activate receptors[1]. Isolated vesicular release events can either occur in response to uncoordinated pacemaker firing[40] or be unrelated to firing, as is the case in RIM cKO^{DA} mice[33,34,41]. Previous work evaluated mice with an attenuation in input-driven increases in firing by removing NMDA receptors from dopamine neurons[37,38]. These mice had decreased burst firing rates, which reduced induced dopamine release, as measured with voltammetry, by about half and had impaired conditioned behavioural responses. The release deficit was milder than in RIM cKO^{DA} mice. A strong phasic response persisted, probably because NMDA receptor removal did not disrupt the synchronizing effects of glutamatergic inputs. Release in response to the remaining phasic firing and to tonic firing were unaffected.

In RIM cKO^{DA} mice, release triggered by action potentials is substantially impaired, which results in reduced dopamine release in response to both phasic and tonic firing. The dopamine release deficit observed in RIM cKO^{DA} mice has previously been characterized using brain slice amperometry and electrophysiology, and with in vivo microdialysis[33–36]. We here expanded on these analyses with fluorescent sensors in brain slices and in vivo. The dopamine sensors have rapid on-kinetics, but the relatively slow off-kinetics and the nature of the bulk photometric measurements may slow signal decay. Although the sensors show overall good specificity, related transmitters such as noradrenaline, which is present in the ventral striatum, may contribute to fluorescence signals[31,47,48]. Fibre photometry reports a bulk signal, and some high local dopamine might escape detection; for example, dopamine reported by brain slice electrophysiology[36] or in response to tonic firing. In any case, ablating RIM strongly decreases action-potential-induced dopamine release. Stochastic activations of small and changing dopamine receptor subsets that can occur in the absence of firing might drive the unaffected dopamine-dependent behaviours. Our work indicates that there are important roles for spontaneous, firing-independent dopamine release. For movement, the distinction between action-potential-dependent and action-potential-independent release is likely to be more important than that of phasic and tonic dopamine neuron activity.

Understanding the mechanisms of L-DOPA is important because patients with Parkinson's disease rely on this treatment. In patients, L-DOPA might work through enhancing tonic dopamine, and sustained-release formulations indeed ameliorate L-DOPA-induced dyskinesias[14,49]. Our work establishes experimentally that L-DOPA can restore spontaneous movement without increasing phasic signals. The action of L-DOPA substantiates that dopamine source and timing are not essential for improving motor function. However, L-DOPA treatment is not effective for all Parkinson's disease symptoms, and side effects develop over time, probably because L-DOPA does not restore the regular modes of dopamine transmission. Aberrant dopamine fluctuations, constant dopamine receptor activations or adaptations in response to these factors might induce dyskinesias.

In contrast to its dispensability for movement initiation, we find that ablating action-potential-induced dopamine release results in substantial deficits in reward-conditioned behaviours. Previous studies have

postulated that reward-based learning involves dopamine-dependent and dopamine-independent mechanisms[50–52]. The disruption of RIM function may manifest in multiple aspects of behaviour, including learning, motivation, action selection, response vigour and skilled movement[7,21,46,53–56]. RIM cKO^{DA} mice can effectively learn to discriminate two odours. By contrast, RIM is important for promoting reward-driven behaviour, and RIM removal reduces trial initiations during odour discrimination and licking during probabilistic cue-reward associations. These results indicate a decrease in motivation. It has been proposed that motivation is mediated by phasic dopamine activities[20,57], and it may be reduced because these dynamics are disrupted after RIM ablation. Alternatively, loss of dopamine release in response to tonic firing in RIM cKO^{DA} mice may reduce motivation (Supplementary Discussion). Our findings complement earlier work in which modulating dopamine signalling through genetic inhibition of re-uptake magnified performance and motivation[58,59]. Moreover, motivation has learned components. This is illustrated by the evolving behavioural response to free water (Fig. 5), and reduced motivation might be related to impaired associative learning.

Our results indicate that diverse mechanisms may mediate learning and expression of anticipatory behaviour in response to reward-predicting cues. Expression of reward anticipation strongly depends on RIM in dopamine neurons (Fig. 5), whereas discrimination of cues to instruct actions is independent of it (Fig. 4). Learning of cue–action associations in these tasks may be distinct. Learning might be dopamine-independent or be supported by baseline dopamine, similar to spontaneous movement. This conclusion is supported by a recent study in which mice with a decrease in train-induced dopamine release through dopamine neuron-specific deletion of VPS41 learned to collect food rewards effectively over a few days of training, albeit with a delay[60]. Although our data implicate that RIM has a role in motivation, they do not exclude that learning of probabilistic rewards relies on precisely timed dopamine action. The impaired anticipatory behaviour after RIM ablation can be caused by a defect in reinforcement learning. The impeded performance during odour discrimination may be caused by impaired learning of skilled movements. The limited temporal control in our genetic experiments makes it difficult to distinguish learning versus performance, and future work should disambiguate these possibilities. Nonetheless, our findings establish distinct roles for dopamine signalling modes in spontaneous movement and reward-conditioned behaviours.

Online content

Any methods, additional references, Nature Portfolio reporting summaries, source data, extended data, supplementary information, acknowledgements, peer review information; details of author contributions and competing interests; and statements of data and code availability are available at https://doi.org/10.1038/s41586-024-08038-z.

1. Liu, C., Goel, P. & Kaeser, P. S. Spatial and temporal scales of dopamine transmission. *Nat. Rev. Neurosci.* **22**, 345–358 (2021).
2. Grace, A. A. Dysregulation of the dopamine system in the pathophysiology of schizophrenia and depression. *Nat. Rev. Neurosci.* **17**, 524–532 (2016).
3. da Silva, J. A., Tecuapetla, F., Paixao, V. & Costa, R. M. Dopamine neuron activity before action initiation gates and invigorates future movements. *Nature* **554**, 244–248 (2018).
4. Howe, M. W. & Dombeck, D. A. Rapid signalling in distinct dopaminergic axons during locomotion and reward. *Nature* **535**, 505–510 (2016).
5. Dodson, P. D. et al. Representation of spontaneous movement by dopaminergic neurons is cell-type selective and disrupted in parkinsonism. *Proc. Natl Acad. Sci. USA* **113**, E2180–E2188 (2016).
6. Jin, X. & Costa, R. M. Start/stop signals emerge in nigrostriatal circuits during sequence learning. *Nature* **466**, 457–462 (2010).
7. Berke, J. D. What does dopamine mean? *Nat. Neurosci.* https://doi.org/10.1038/s41593-018-0152-y (2018).
8. Coddington, L. T. & Dudman, J. T. Learning from action: reconsidering movement signaling in midbrain dopamine neuron activity. *Neuron* **104**, 63–77 (2019).
9. Schultz, W. Multiple dopamine functions at different time courses. *Annu. Rev. Neurosci.* **30**, 259–288 (2007).
10. Schultz, W., Dayan, P. & Montague, P. R. A neural substrate of prediction and reward. *Science* **275**, 1593–1599 (1997).
11. Kim, H. R. et al. A unified framework for dopamine signals across timescales. *Cell* **183**, 1600–1616.e25 (2020).
12. Amo, R. et al. A gradual temporal shift of dopamine responses mirrors the progression of temporal difference error in machine learning. *Nat. Neurosci.* **25**, 1082–1092 (2022).
13. Watabe-Uchida, M., Eshel, N. & Uchida, N. Neural circuitry of reward prediction error. *Annu. Rev. Neurosci.* **40**, 373–394 (2017).
14. Poewe, W. et al. Parkinson disease. *Nat. Rev. Dis. Primers* **3**, 17013 (2017).
15. Cotzias, G. C., Van Woert, M. H. & Schiffer, L. M. Aromatic amino acids and modification of parkinsonism. *N. Engl. J. Med.* **276**, 374–379 (1967).
16. Carlsson, A. A paradigm shift in brain research. *Science* **294**, 1021–1024 (2001).
17. Carlsson, A. On the problem of the mechanism of action of some psychopharmaca. *Psychiatr. Neurol.* **140**, 220–222 (1960).
18. Bakhurin, K. et al. Force tuning explains changes in phasic dopamine signaling during stimulus-reward learning. Preprint at *bioRxiv* https://doi.org/10.1101/2023.04.23.537994 (2023).
19. Jeong, H. et al. Mesolimbic dopamine release conveys causal associations. *Science* **378**, eabq6740 (2022).
20. Berridge, K. C., Robinson, T. E. & Aldridge, J. W. Dissecting components of reward: 'liking', 'wanting', and learning. *Curr. Opin. Pharmacol.* **9**, 65–73 (2009).
21. Niv, Y., Daw, N. D., Joel, D. & Dayan, P. Tonic dopamine: opportunity costs and the control of response vigor. *Psychopharmacology* **191**, 507–520 (2007).
22. Hamilos, A. E. et al. Slowly evolving dopaminergic activity modulates the moment-to-moment probability of reward-related self-timed movements. *eLife* **10**, e62583 (2021).
23. Mohebi, A. et al. Dissociable dopamine dynamics for learning and motivation. *Nature* **570**, 65–70 (2019).
24. Howe, M. et al. Coordination of rapid cholinergic and dopaminergic signaling in striatum during spontaneous movement. *eLife* **8**, e44903 (2019).
25. Yagishita, S. et al. A critical time window for dopamine actions on the structural plasticity of dendritic spines. *Science* **345**, 1616–1620 (2014).
26. Chaudhury, D. et al. Rapid regulation of depression-related behaviours by control of midbrain dopamine neurons. *Nature* **493**, 532–536 (2013).
27. Crego, A. C. G. et al. Complementary control over habits and behavioral vigor by phasic activity in the dorsolateral striatum. *J. Neurosci.* **40**, 2139–2153 (2020).
28. Bova, A. et al. Precisely timed dopamine signals establish distinct kinematic representations of skilled movements. *eLife* **9**, e61591 (2020).
29. Howard, C. D., Li, H., Geddes, C. E. & Jin, X. Dynamic nigrostriatal dopamine biases action selection. *Neuron* **93**, 1436–1450.e8 (2017).
30. Liu, C. et al. An action potential initiation mechanism in distal axons for the control of dopamine release. *Science* **375**, 1378–1385 (2022).
31. Sun, F. et al. Next-generation GRAB sensors for monitoring dopaminergic activity in vivo. *Nat. Methods* **17**, 1156–1166 (2020).
32. Patriarchi, T. et al. An expanded palette of dopamine sensors for multiplex imaging in vivo. *Nat. Methods* **17**, 1147–1155 (2020).
33. Liu, C., Kershberg, L., Wang, J., Schneeberger, S. & Kaeser, P. S. Dopamine secretion is mediated by sparse active zone-like release sites. *Cell* **172**, 706–718.e15 (2018).
34. Banerjee, A. et al. Molecular and functional architecture of striatal dopamine release sites. *Neuron* **110**, 248–265.e9 (2022).
35. Robinson, B. G. et al. RIM is essential for stimulated but not spontaneous somatodendritic dopamine release in the midbrain. *eLife* **8**, e47972 (2019).
36. Zych, S. M. & Ford, C. P. Divergent properties and independent regulation of striatal dopamine and GABA co-transmission. *Cell Rep.* **39**, 110823 (2022).
37. Parker, J. G. et al. Absence of NMDA receptors in dopamine neurons attenuates dopamine release but not conditioned approach during Pavlovian conditioning. *Proc. Natl Acad. Sci. USA* **107**, 13491–13496 (2010).
38. Zweifel, L. S. et al. Disruption of NMDAR-dependent burst firing by dopamine neurons provides selective assessment of phasic dopamine-dependent behavior. *Proc. Natl Acad. Sci. USA* **106**, 7281–7288 (2009).
39. Grace, A. A. & Bunney, B. S. The control of firing pattern in nigral dopamine neurons: burst firing. *J. Neurosci.* **4**, 2877–2890 (1984).
40. Grace, A. A. & Bunney, B. S. The control of firing pattern in nigral dopamine neurons: single spike firing. *J. Neurosci.* **4**, 2866–2876 (1984).
41. Banerjee, A., Lee, J., Nemcova, P., Liu, C. & Kaeser, P. S. Synaptotagmin-1 is the Ca^{2+} sensor for fast striatal dopamine release. *eLife* **9**, e58359 (2020).
42. Ungerstedt, U. Postsynaptic supersensitivity after 6-hydroxy-dopamine induced degeneration of the nigro-striatal dopamine system. *Acta Physiol. Scand. Suppl.* **367**, 69–93 (1971).
43. Keefe, K. A., Salamone, J. D., Zigmond, M. J. & Stricker, E. M. Paradoxical kinesia in parkinsonism is not caused by dopamine release. Studies in an animal model. *Arch. Neurol.* **46**, 1070–1075 (1989).
44. Lebowitz, J. J. et al. Synaptotagmin-1 is a Ca^{2+} sensor for somatodendritic dopamine release. *Cell Rep.* **42**, 111915 (2023).
45. German, P. W. & Fields, H. L. Rat nucleus accumbens neurons persistently encode locations associated with morphine reward. *J. Neurophysiol.* **97**, 2094–2106 (2007).
46. Tsutsui-Kimura, I. et al. Distinct temporal difference error signals in dopamine axons in three regions of the striatum in a decision-making task. *eLife* **9**, e62390 (2020).
47. Berridge, C. W., Stratford, T. L., Foote, S. L. & Kelley, A. E. Distribution of dopamine β-hydroxylase-like immunoreactive fibers within the shell subregion of the nucleus accumbens. *Synapse* **27**, 230–241 (1997).
48. Schroeter, S. et al. Immunolocalization of the cocaine- and antidepressant-sensitive L-norepinephrine transporter. *J. Comp. Neurol.* **420**, 211–232 (2000).
49. Antonini, A. et al. Effect of levodopa–carbidopa intestinal gel on dyskinesia in advanced Parkinson's disease patients. *Mov. Disord.* **31**, 530–537 (2016).
50. Flagel, S. B. et al. A selective role for dopamine in stimulus-reward learning. *Nature* **469**, 53–57 (2011).
51. Dolan, R. J. & Dayan, P. Goals and habits in the brain. *Neuron* **80**, 312–325 (2013).

52. Wang, J. X. et al. Prefrontal cortex as a meta-reinforcement learning system. *Nat. Neurosci.* **21**, 860–868 (2018).
53. Wang, A. Y., Miura, K. & Uchida, N. The dorsomedial striatum encodes net expected return, critical for energizing performance vigor. *Nat. Neurosci.* **16**, 639–647 (2013).
54. Dudman, J. T. & Krakauer, J. W. The basal ganglia: from motor commands to the control of vigor. *Curr. Opin. Neurobiol.* **37**, 158–166 (2016).
55. Seiler, J. L. et al. Dopamine signaling in the dorsomedial striatum promotes compulsive behavior. *Curr. Biol.* **32**, 1175–1188.e5 (2022).
56. van Elzelingen, W. et al. Striatal dopamine signals are region specific and temporally stable across action-sequence habit formation. *Curr. Biol.* **32**, 1163–1174.e6 (2022).
57. Wyvell, C. L. & Berridge, K. C. Intra-accumbens amphetamine increases the conditioned incentive salience of sucrose reward: enhancement of reward 'wanting' without enhanced 'liking' or response reinforcement. *J. Neurosci.* **20**, 8122–8130 (2000).
58. Cagniard, B. et al. Dopamine scales performance in the absence of new learning. *Neuron* **51**, 541–547 (2006).
59. Yin, H. H., Zhuang, X. & Balleine, B. W. Instrumental learning in hyperdopaminergic mice. *Neurobiol. Learn. Mem.* **85**, 283–288 (2006).
60. Jain, S. et al. Adaptor protein-3 produces synaptic vesicles that release phasic dopamine. *Proc. Natl Acad. Sci. USA* **120**, e2309843120 (2023).

Methods

Mice

Conditional RIM1 (ref. 61) and RIM2 (ref. 62) knockout mice (RIM1^{floxed}, *Rims1* gene targeted, RRID: IMSR_JAX:015832; RIM2^{floxed}, *Rims2* gene targeted, RRID: IMSR_JAX:015833) or conditional synaptotagmin-1 (Syt-1, also called SYT1)[63] knockout mice (Syt-1^{floxed}, *Syt1* gene targeted, RRID: IMSR_EM:06829) were crossed to *Dat*$^{Ires\text{-}cre}$ mice[64] (*Slc6a3* gene targeted, RRID: IMSR_JAX:006660) as previously established[33,41]. For conditional knockout experiments, mice heterozygous for *Dat*$^{Ires\text{-}cre}$ and homozygous for floxed RIM1 and RIM2 were used as RIM cKO^{DA} mice. RIM control mice were from the same crossings and had heterozygote floxed RIM1, RIM2 and *Dat*$^{Ires\text{-}cre}$ alleles as previously described[33,34]. Mice heterozygous for *Dat*$^{Ires\text{-}cre}$ and homozygous for floxed Syt-1 were used as Syt-1 cKO^{DA} mice. Syt-1 control mice were from the same crossings and were heterozygous *Dat*$^{Ires\text{-}cre}$ and wild type for Syt-1. For L-DOPA restoration of movement in control mice (Fig. 3b–j and Extended Data Figs. 8h–j and 9a–e), Syt-1 control mice (which are heterozygous for *Dat*$^{Ires\text{-}cre}$) were used. Mice heterozygous for *Dat*$^{Ires\text{-}cre}$ were used in Extended Data Fig. 2d–l (one cohort) and in Extended Data Figs. 7 and 8b–g (another cohort). Surgeries were started at 30 days of age (80 ± 48 days; mean ± s.d.) and experiments were completed at 122 ± 67 days of age. Specifically, the following age ranges (mean ± s.d.) for completion of experiments were used: 120 ± 71 days for Fig. 1a–d and Extended Data Figs. 1a–i and 10a–d; 135 ± 78 days for Fig. 1e–t and Extended Data Fig. 1j–af; 105 ± 50 days for Fig. 2 and Extended Data Figs. 2–5; 92 ± 54 days for Fig. 3 and Extended Data Figs. 6–9; 103 ± 11 days for Fig. 4; and 203 ± 21 days for Fig. 5 and Extended Data Fig. 10e–s. Mice used in behavioural experiments were housed in a reversed 12-h light–dark cycle in rooms set to 21–24 °C and 50% humidity, and behavioural experiments were conducted during the dark phase of the cycle. For slice imaging and behavioural experiments, the mice were either littermate pairs or age-matched pairs from the respective crossings because it was not always possible to obtain full cohorts of littermate pairs owing to the complexity of the genetic experiments. Female and male mice were included in all experiments irrespective of sex. Genotype comparisons in brain slice and behavioural experiments were performed by an experimenter blind to the genotype throughout data acquisition and analyses. For L-DOPA restoration of movement in Fig. 3, the experimenter was blind to the condition during data analyses. Animal experiments were performed in accordance with approved protocols of the Harvard University Animal Care and Use Committee.

Drugs

Drugs were injected (i.p.) with a total volume of less than 0.15 ml. Reserpine was dissolved in dimethyl sulfoxide (DMSO) and administered at 2 mg kg^{-1} (open-field experiments in Fig. 1) or 3 mg kg^{-1} (open-field experiments with reserpine and L-DOPA methyl ester or carbidopa restoration of movement in Fig. 3 and Extended Data Figs. 8h–j and 9). SCH23390 (in PBS) and haloperidol (in DMSO) were injected at a final concentration of 1 mg kg^{-1} and 2 mg kg^{-1}, respectively (open-field experiments in Fig. 1). Haloperidol (in DMSO) was injected at 2 mg kg^{-1} (fibre photometry experiments in Extended Data Figs. 3 and 6) and apomorphine (in PBS) was injected at 1 mg kg^{-1} (Extended Data Figs. 1ac,ad and 4d–f). For experiments in Fig. 3 and Extended Data Figs. 7–9, 250 mg kg^{-1} L-DOPA methyl ester (in 0.01% ascorbic acid) was injected together with 25 mg kg^{-1} carbidopa (in 0.01% ascorbic acid). For unilateral lesion of dopamine axons, 1 µl of a solution with 3.5 µg µl^{-1} of 6-OHDA (in 0.02% ascorbic acid) was injected stereotaxically as described below, and apomorphine-induced rotations were assessed 3 weeks after surgery. For drug infusion into the brain, drugs were delivered in a total volume of 1 µl using a syringe pump at 0.2 µl min^{-1}. Drugs were dissolved in artificial cerebrospinal fluid (ACSF) containing (in mM): 155 NaCl, 1.2 $CaCl_2$, 1.2 $MgCl_2$, 2.5 KCl and 5 glucose heated to 37 °C before use. SCH23390 and haloperidol were infused at a final concentration of 20 µM and 40 µM, respectively (Extended Data Fig. 2). Tetrodotoxin (TTX; in ACSF) was infused at a concentration of 500 nM in the dorsal striatum during fibre photometry (Extended Data Fig. 2).

Stereotaxic surgeries

Surgeries in mice for slice imaging or for open-field experiments were adapted from previously established methods[30] and conducted unilaterally in the right striatum or bilaterally (Extended Data Fig. 2). Anaesthesia was induced with 5% isoflurane and mice were mounted on a stereotaxic frame; 1.5–2% isoflurane was used to maintain stable anaesthesia during surgery. After exposing the skull, a small hole was drilled and adeno-associated viruses (AAVs) were injected using a microinjector pump into the SNc (1.1 mm anterior, 1.3 mm lateral of Lambda and 4.2 mm below the pia) or into the dorsal striatum (1.0 mm anterior, 2.0 mm lateral of Bregma and 2.5 mm below the pia) and/or into the ventral striatum (1.45 mm anterior, 1.4 mm lateral of Bregma and 4.35 mm below the pia). A total volume of 1 µl virus diluted to a titre of 10^{12}–10^{13} genomic copies per ml was injected at a rate of 0.1 µl min^{-1}, and the microinjector was left for an additional 10 min after injection. In mice for open-field experiments with fibre photometry, an optical cannula (400 µm diameter, Doric) was implanted immediately after virus injection in the dorsal striatum (1.0 mm anterior, 2.0 mm lateral of Bregma and 2.4 mm below the pia) and was secured by two bone screws. The cannula and screws were fixed to the skull using fast-curing optical adhesive and dental cement. For locomotion tests with infusion of drugs in the brain, dual-fluid cannulas (530 µm diameter, Doric) were implanted bilaterally (dorsal striatum, coordinates: 1.0 mm anterior, 2.0 mm lateral of Bregma and 2.4 mm below the pia). For fibre photometry combined with drug infusion, an opto-fluid cannula (400 µm in diameter, Doric) was implanted immediately after virus injection (dorsal striatum, coordinates: 1.0 mm anterior, 2.0 mm lateral of Bregma and 2.4 mm below the pia). Unilateral lesion of dopamine axons was performed by injecting 1 µl 6-OHDA (3.5 µg µl^{-1}) into the right medial forebrain bundle (1.0 mm posterior, 1.0 mm lateral of Bregma and 4.9 mm below the pia). Surgeries in mice for head-fixed experiments were adapted from previously established methods[12]. Mice were anaesthetized with 3% isoflurane for induction, were mounted on a stereotaxic frame and anaesthesia was maintained at 1–2% isoflurane. A local anaesthetic (1:1 mixture of 2% lidocaine and 0.5% bupivacaine) was subcutaneously injected at the incision site. A custom-made head-plate was attached to the cleaned and dried skull with adhesive cement containing charcoal powder. AAVs were injected using a glass pipette into the left ventral striatum (1.45 mm anterior, 1.4 mm lateral of Bregma and 4.35 mm below pia) and into the right dorsal striatum (1.0 mm anterior, 2.0 mm lateral of Bregma and 2.5 mm below pia). A volume of 1 µl virus (at each injection site) diluted to a titre of 10^{12}–10^{13} genomic copies per ml was manually injected into the left ventral striatum and into the right dorsal striatum. The injection rate was about 0.1 µl min^{-1}, and the glass pipette was left for an additional 10 min after injection. Optical cannulas (400 µm in diameter, Doric) were implanted immediately after virus injection in the left ventral striatum (1.45 mm anterior, 1.4 mm lateral of Bregma and 4.15 mm below the pia) and the right dorsal striatum (1.0 mm anterior, 2.0 mm lateral of Bregma and 2.35 mm below the pia) and fixed to the skull with adhesive cement containing charcoal powder. Mice in both types of surgeries were treated for postsurgical pain and were returned to home cages after completion of the surgery. Mice were used for experiments starting 5 days (drug infusions) or 20 days (if AAVs were injected) and up to 141 days after surgery. Cannula positions were confirmed by histology post hoc in 61 (of a total of 71) mice with implanted cannulas and are provided in Supplementary Fig. 5. A few mice early in the project were euthanized without a histological assessment. For histological analyses, mice were perfused using 4% paraformaldehyde (PFA) and cannulas were removed. The brains were dissected out and kept in 4% PFA until processing. Brains were sliced coronally at 100 µm

with a vibratome and mounted on glass slides in mounting medium. Bright-field and fluorescence images were acquired using an Olympus VS120 slide scanner, and cannula positions were determined from the cannula track and mapped following anatomical landmarks using the Allen Brain Atlas[65] as a reference.

AAVs

For measuring dopamine release in brain slices, AAV9-hSyn-GRAB$_{DA2m}$ (ref. 31) (purchased from WZ Bioscience with permission of Y.L., injected at 2–6 × 10^{12} copies per ml) was injected into the dorsal or ventral striatum. To visualize dopamine dynamics in vivo with fibre photometry, AAV9-hSyn-GRAB$_{DA2m}$ and AAV9-CAG-tdTomato (purchased from the Boston Children's Hospital Viral Core or from Addgene, 59462-AAV9, injected at 1–2 × 10^{12} copies per ml) were injected together in the dorsal or ventral striatum. To visualize Ca^{2+} dynamics in dopamine axons, AAV9-CAG-Flex-GCaMP6s[66] (purchased from Addgene, 100842-AAV9, injected at 2–3 × 10^{12} copies per ml) and AAV9-CAG-tdTomato were injected together into the SNc of mice heterozygous for *Dat*$^{Ires\text{-}cre}$. To monitor dopamine axon activity and dopamine dynamics simultaneously, AAV9-CAG-Flex-GCaMP6s was injected into the SNc, and AAV9-hSyn-RdLight1 (ref. 32) (obtained from T.P., injected at 2–3 × 10^{12} copies per ml) was injected into the dorsal striatum of mice heterozygous for *Dat*$^{Ires\text{-}cre}$.

Slice imaging

Dopamine release in brain slices was measured following previously established methods[30]. AAV9-hSyn-GRAB$_{DA2m}$ was injected into the dorsal or ventral striatum of mice. At 20–35 days after injection, the mice were deeply anaesthetized with isoflurane and decapitated. Parasagittal mouse brain slices containing the striatum (250-µm thick) were cut using a vibratome (Leica) in an ice-cold cutting solution containing (in mM): 75 NaCl, 2.5 KCl, 7.5 $MgSO_4$, 75 sucrose, 1 NaH_2PO_4, 12 glucose, 26.2 $NaHCO_3$, 1 myo-inositol, 3 pyruvic acid and 1 ascorbic acid. Slices were then incubated at room temperature in an incubation solution containing (in mM): 126 NaCl, 2.5 KCl, 2 $CaCl_2$, 1.3 $MgSO_4$, 1 NaH_2PO_4, 12 glucose, 26.2 $NaHCO_3$, 1 myo-inositol, 3 pyruvic acid and 1 ascorbic acid for at least 1 h before use. Imaging was performed in a chamber continuously perfused with ACSF containing (in mM): 126 NaCl, 2.5 KCl, 2 $CaCl_2$, 1.3 $MgSO_4$, 1 NaH_2PO_4, 12 glucose and 26.2 $NaHCO_3$ heated to 30–36 °C at 2.5–3.0 ml min^{-1}. All solutions were constantly bubbled with 95% O_2 and 5% CO_2, and experiments were completed within 5 h after slicing. Fluorescence imaging was performed using an Olympus BX51 epi-fluorescence microscope. Fluorescent probes were excited with a 470 nm LED, and signals were collected through a ×4 objective and digitized with a scientific complementary metal-oxide-semiconductor camera (sCMOS, Hamamatsu ORCA-Flash4.0). Dopamine release was induced using electrical stimulation applied through a unipolar glass pipette (tip diameter of 3–5 µm) filled with ACSF. Electrical stimulation was delivered as a single stimulus, as two stimuli at 1 Hz or as 10 stimuli at 10 Hz. A biphasic wave (0.25 ms in each phase) was applied for stimulation, and stimulation intensity was set to 90 µA. The stimulus was applied with a linear stimulus isolator (A395, World Precision Instruments) and controlled with a digitizer (Molecular Devices, Digidata 1440A). Responses were acquired at 512 × 512 pixels per frame, 50 frames per s, with an exposure time of 20 ms. Each pixel represents a physical area of 5.4 × 5.4 $µm^2$ (Fig. 1a–d) or 6.4 × 6.4 $µm^2$ (Extended Data Fig. 10a–d). For image analyses, regions of interest containing the signal in the dorsal or ventral striatum were manually selected in each image stack, and the background in each image frame was estimated from cortical regions where no sensor was expressed and subtracted. For quantification of induced release, F_0 was estimated as the average fluorescence signal over 0.5 s immediately before stimulation. $\Delta F/F_0$ was calculated for each pixel, and pixels with a $\Delta F/F_0 > 0.02$ in response to electrical stimulation were considered part of a release event. The product of $\Delta F/F_0$ and of the area above the $\Delta F/F_0 > 0.02$ threshold in each frame was calculated to generate plots for quantitative comparison. The cut-off of 0.02 was selected based on the background noise level in regions with low baseline fluorescence. Example images were generated by calculating the average $\Delta F/F_0$ at 20–100 ms after stimulation of the background-subtracted image stack, and the colour range in the resulting images was adjusted using identical settings within an experiment.

Slice amperometry

Slice amperometry was performed following established methods[33,34]. Parasagittal mouse brain slices were prepared as described in slice imaging. Carbon-fibre microelectrodes (CFEs; 7 µm in diameter and 200–350 µm in length, made from carbon fibre filament, Goodfellow) were calibrated before use by puffing freshly made dopamine solutions, and a new CFE was used on each day. Amperometry was performed in a chamber continuously perfused with ACSF containing (in mM): 126 NaCl, 2.5 KCl, 2 $CaCl_2$, 1.3 $MgSO_4$, 1 NaH_2PO_4, 12 glucose and 26.2 $NaHCO_3$ heated to 30–35 °C at 2.5–3 ml min^{-1}. The CFE was held at a constant voltage of 600 mV and positioned in the dorsal striatum as indicated in Extended Data Fig. 1a at one of three locations (near the cortex, near the globus pallidus or near the hippocampus). To assess TTX sensitivity, recordings were performed before and after the addition of 1 µM TTX in ACSF (10 min of incubation, no stimulation during the incubation time). For genotype comparisons, a RIM control mouse and RIM cKO^{DA} mouse were used on a single day and slices were interleaved. Signals were acquired using an amplifier (Molecular Devices, Multiclamp 700B), low-pass filtered at 400 Hz and digitized (Molecular Devices, Digidata 1440A). Electrical stimulation was carried out with an ACSF-filled glass pipette (tip diameter of 3–5 µm) and was delivered as a single stimulus at 90 µA intensity with a biphasic wave (0.25 ms in each phase) every 2 min. The electrode was placed 100–150 µm away from the CFE. The peak of the amperometric response generally appeared around 10 ms after the electrical stimulus and was quantified in a time window that ended around 100 ms after the stimulus. The peak dopamine concentration was calculated based on the CFE calibration. The stimulus artefact ended within the first few ms of the electrical stimulus and was excluded from the peak analysis.

Analysis of gait

Gait analyses were performed as previously described[67]. Mice moved in a transparent linear corridor that was 64.5 cm long, 4 cm wide and 6 cm high with mirrors installed on each side. The corridor was illuminated by infrared light, and five trials per mouse per day were recorded for eight consecutive days. The bottom view and two side views of mice walking were captured simultaneously by a video camera (Bonito CL-400B/C 2,320 × 700 pixels, Allied Vision) at 200 Hz. The body parts (nose, left and right fore paws, left and right hind paws, rear-end and tail tip) were tracked in the videos using a convolutional neural network based on the stacked hour-glass-network[68] trained with 500 manually labelled frames. A hidden Markov model was used to segregate individual gait cycles. Gait cycles in which body parts were mislabelled or during which mice paused or stepped backwards were excluded post hoc during manual cross-checking by an experimenter blind to the genotype. The following parameters were measured: cadence, the number of cycles per second; stride length, the maximum travelled distance of a fore paw within a single cycle; fore and hind paw width, the lateral distance between the fore paws or the hind paws; velocity, the average speed of the centre of the mouse (calculated as the distance between the nose and the rear-end along the axis of the corridor) within a single gait cycle; tail and rear height, the absolute height of the tail-tip and rear-end from the floor; and tail and rear fluctuation, the standard deviation of the tail and rear movement (horizontal or vertical). The stride length, paw widths, tail and rear heights and fluctuations were normalized to the body length. For statistics, gait parameters were averaged by cycles and mouse.

Horizontal bar test

Mice were placed at one end of a wooden bar (3.2 cm in diameter, 143.8 cm long) positioned 91 cm above the floor. On the first and second days, mice were trained to cross the bar 4 times with an interval of 60 s each day. On the third day, mice were tested for two consecutive experimental trials, and the average time used to travel for 80 cm from the starting point was used for comparison across mice.

Vertical bar test

A vertical plastic pole (0.83 cm in diameter, 50 cm high) was installed in a clean mouse cage. Mice were placed with their heads oriented upwards at the top of the pole, and the total time taken for the mouse to turn and climb down to the bottom of the pole was measured. Mice were trained 4 times with an interval of 60 s each day for 2 days. Two test trials were performed on the third day and all tested mice successfully descended the vertical pole. The average time of the two trials was used for comparison across mice.

Rotarod test

The time the mice can stay on an accelerating rotarod (Harvard Apparatus) was assessed. Mice were trained in 4 daily 60 s sessions for 4 consecutive days at a constant speed of 10 r.p.m. on day 1 and of 24 r.p.m. for days 2–4. On the fifth day, each mouse was tested in two trials at speeds increasing from 5 to 40 r.p.m. at 5 r.p.m., with increments for 60 s at each speed. The time the mice were able to stay on the rotarod was measured, and the average of the two trials for each mouse was used.

Video tracking during open-field exploration

Experiments were performed following previously established methods[30]. Mice were allowed to move freely (between 30 and 90 min depending on the experiment) in a round arena (43.1 cm in diameter, 35.6 cm high) illuminated by a LED (535 nm, 4 μW cm^{-2} measured at the bottom of area), and videography was performed with a CCD camera (Flir, BFLY-U3-05S2M-CS) at a frame rate of 50 Hz (Fig. 1l,m,p–t) or with a high-sensitivity CMOS camera (Thorlabs, DCC3240N) at 25 Hz (other figures). For movement analyses, the snout, left ear, right ear and tail base were tracked in videos using DeepLabCut for markerless pose estimation[69,70] (training network: 50-layer ResNet-50). The algorithm was trained after manually labelling a total of >800 frames extracted from all videos in each experiment, and frames with tracking confidence levels >0.99 were used for analyses. For trajectory plots and analyses of distance travelled, the head centre (defined as the centre point between the snout and the ears) was used. The position of each body part was first smoothed using a moving average with a time window that was 60–240 ms long depending on the acquisition frame rate. Distance travelled was analysed during the first 30 min of videography unless noted otherwise. For the L-DOPA restoration of movement in Fig. 3 and Extended Data Fig. 9, the videography (with or without fibre photometry) began when spontaneous movement in the mice with reserpine-induced bradykinesia started recovering (typically 90–120 min after L-DOPA injection), and distance travelled was analysed for the 31–60 min videography time window. For movement initiation detection in Fig. 1, instant snout velocity was calculated and smoothed using a moving average with a window of 75 ms. Movement initiations were defined as transitions from a low mobility state (velocity amplitude <1× s.d. of the mean velocity and 25 mm s^{-1} for at least 400 ms) to a high mobility state (velocity amplitude >1× s.d. of the mean velocity and 25 mm s^{-1} for at least 80 ms). Peak speed was extracted from the averaged movement initiations across trials for each mouse. Specifically, the maximum value within a time window of 0–400 ms was extracted for each mouse and plotted. The duration of a movement event was defined as the time during which the speed amplitude was above the high mobility state threshold. Peak speed was defined as the maximum speed amplitude of a movement event. For the frequency plots, all events from an animal that were above a specific value for speed or duration were averaged and plotted.

Fibre photometry in freely moving mice

Fibre photometry recordings during locomotion in an open field were in essence performed as previously described[30]. Mice were connected to an optic fibre (400 μm diameter, Doric) and then allowed to move freely (between 30 and 90 min depending on the experiment) in a round arena (43.1 cm in diameter, 35.6 cm high) illuminated by infrared light (850 nm, 30 μW cm^{-2}). A custom-built fibre photometry system was used[30]. The detected fluorescence signals were converted to electrical signals using silicon photodiodes (SM1PD1A, Thorlabs). Electrical signals were amplified by photodiode amplifiers (PDA200C, Thorlabs) and collected by a multifunction I/O card (PCIe-6321, National Instruments) at 10,000 Hz. The channels (470 nm and 565 nm LEDs) were turned on in an alternating pattern at 25 Hz, with each channel being active for 10 ms of the 40 ms period, and the average output of each channel during the 10 ms active time window was assessed. In each experiment, the light power at the fibre end was adjusted such that the detection was in an optimal working range (0.6–1.3 F_0 for green fluorophores; 0.4–0.8 F_0 for red fluorophores) before starting the measurements. The following light power ranges were used: at 470 nm, 120–160 μW for $GRAB_{DA}$, 220–270 μW for GCaMP6s; at 565 nm, 620–670 μW for RdLight1, 6–12 μW for tdTomato (Extended Data Fig. 2d–g). Photometry signals and videography were collected simultaneously using a TTL control at 25 Hz. During fibre photometry recordings, 200 ms light pulses were applied at random time intervals ranging from 100 to 900 s (565 nm LED light source, 50 μW cm^{-2} measured at the bottom of the arena) to illuminate the open-field arena, and these light pulses were also used to calibrate and confirm correct alignment of photometry and videography data. For drug injections, mice were removed from the arena by hand and returned after injection without interrupting the recording. For analyses, the raw photometry signal F was first processed with a low-pass filter at 0.01 Hz to estimate F_0, and $\Delta F/F_0$ was calculated. To compare F_0 across conditions, the mean F_0 value of the time window from 40 s to 260 s of each recording session was calculated; plots of all F_0 values are provided in Supplementary Fig. 6. If a mouse underwent multiple recording sessions, the mean F_0 was calculated from a randomly selected session for F_0 comparison. For movement analyses, body parts (snout, left ear, right ear and tail base) were tracked in videos using DeepLabCut[69,70] (training network: 50-layer ResNet-50) trained with >800 manually labelled frames randomly extracted from all videos within the experiment. Only video frames with tracking confidence levels >0.99 were used for further analyses, and frames 200 ms before and after the light pulses were excluded from the analyses. For each frame, head orientation was determined by drawing an axis from the midpoint between the two ears and the snout. Snout velocity was calculated for each frame using the snout displacement between the previous and subsequent frames, and the relative angle of velocity and head orientation was then calculated for each time point. For $\Delta F/F_0$ polar coordinate plots in Figs. 2h and 3f and Extended Data Figs. 3d and 9a, velocity vectors and their corresponding $\Delta F/F_0$ were calculated for each frame and each animal over the course of the videography. Velocities for which amplitude and angle appeared less than 4 times during the recording were considered rare events and were excluded. The plots were generated by registering $\Delta F/F_0$ onto the corresponding position defined by the velocity vectors in polar coordinates. For each animal, the image was then downsampled to 51 × 51 (Fig. 2h and Extended Data Fig. 3d) or 41 × 41 (Fig. 3f and Extended Data Fig. 9a) pixels, and the final plot was generated by averaging images across animals. The shifting of the time course in Extended Data Figs. 3d and 9a was done by artificially advancing (−80 to −400 ms, 80 ms increments) or delaying (80 to 400 ms, 80 ms increments) the velocity time course relative to the photometry signal followed by generation of polar coordinate plots

for each shift. For the alignment of photometry signals to movement initiation, movement initiation events were defined as a period of rest (velocity amplitude <2× s.d. of the mean velocity and 25 mm s^{-1} for at least 400 ms for $GRAB_{DA}$ datasets, GCaMP6s and RdLight1 datasets in experiments in RIM control and RIM cKO^{DA} mice and for reserpine plus L-DOPA rescue experiments) followed by a period of motor activity (velocity amplitude >2× s.d. of the mean velocity and 25 mm s^{-1} for at least 120 ms for $GRAB_{DA}$ datasets, GCaMP6s and RdLight1 datasets in RIM control and RIM cKO^{DA} mice and for reserpine plus L-DOPA rescue with $GRAB_{DA}$ experiments in $DAT^{IRES\text{-}cre}$ mice). For the analysis of left and right turns, movement events with velocity angles between 0° and 180° (left turns, contralateral to imaging) or between 180° and 360° (right turns, ipsilateral to imaging) were grouped together. For movement events and corresponding photometry signals, the average baseline (40 to 440 ms before movement onset) of all mice within the same group was subtracted and heatmaps were generated; for summary time course plots, events were averaged. For peak plots, velocity and $\Delta F/F_0$ were averaged across trials for each mouse and the maximum value within a predefined time window (0–400 ms for velocity, 0–600 ms for $GRAB_{DA}$ $\Delta F/F_0$ or GCaMP6s $\Delta F/F_0$ or RdLight1 $\Delta F/F_0$) was extracted for each mouse, averaged and plotted. For Extended Data Fig. 5c, cross-correlation was performed between GCaMP6s and RdLight1 with RdLight1 as the reference signal. For Extended Data Fig. 5f, the area under the curve was integrated from 0 to 600 ms. The regression was calculated using events with a GCaMP6s area between −4 and 8 $\Delta F/F_0 \times$ s.

Food-CPP

Food-CPP was assessed by adapting a previously described method[71]. Mice were habituated to handling for 3 days before food-CPP; on each day, each mouse was hand-held for 10 min. The custom-built CPP arena had three compartments: two side compartments (20 × 20 × 20 cm^3) and a smaller middle compartment (20 × 10 × 10 cm^3). The compartments were connected by small, semicircular openings (10 cm in diameter). The two side compartments had distinct floors and colour patterns on walls. The CPP arena was illuminated by LED light sources (white light, 1.7–2 μW cm^{-2} measured at the floor each compartment, and infrared light, 850 nm, 13–17 μW cm^{-2} measured at the floor each compartment) and a camera was mounted on top. On day 1, the mouse was placed in the CPP arena in one of the side rooms and the mouse explored the CPP arena for 20 min. The compartment that was less preferred on day 1 was used as the food compartment on the subsequent days. On day 2 (conditioning), the mouse was first confined to the preferred compartment for 15 min. The mouse was then placed in the less-preferred compartment with scattered chocolate food pellets (about 8 g) for 15 min. On day 3 (test), the mouse was allowed to explore all three compartments for 20 min. The conditioning-and-test cycle of days 2 and 3 was repeated three more times, keeping the food compartment the same. For analyses, the snout, left ear, right ear and tail base were tracked in videos using DeepLabCut[69,70] (training network: 50-layer ResNet-50). The algorithm was trained after manually labelling a total of 3,764 frames randomly extracted from all videos in the experiment, and only frames with tracking confidence levels >0.99 were used for analyses. The centre of the head (defined as the centre point between the snout and the ears) was used to determine mouse position. The preference for the food-associated compartment was quantified as the time spent on the side with food pellets on the preceding day. Centre entries were defined as the mouse accessing the middle compartment from either of the side rooms and were averaged for each day and each mouse. The heatmaps illustrate the relative amount of time a mouse spent at each location in a recording session, and the enhanced centre presence reflects mice moving through the openings located in the centre. To generate the heatmaps, a local sum was generated and blurred using box filtering. The speed of the centre entries was calculated using position changes of the head centre for each mouse in two consecutive frames.

Two odour discrimination

Mice were placed on a restricted water schedule and were subjected to a two odour discrimination task in a custom-built behavioural box (32 × 19 × 30 cm^3) with a NIDAQ board (National Instruments) to control tasks as previously established[46]. Before assessment in the two odour discrimination task, mice underwent a shaping period and first practiced poking their nose into the left or right reward port to obtain a water reward. Mice were then required to poke into the centre port (which triggered the delivery of an odour) before entering into a reward port. The required duration for a centre poke was gradually increased to 100 ms. Mice were subjected to this condition until they completed more than 20 valid trials per session in which the duration of the centre poke was >100 ms and was followed by a poke into one of the side ports. After learning this process, mice were subjected to a two odour discrimination task[72]. In the task, mice initiated a trial by poking their nose into a centre port. Different odours (odour A or odour B) were delivered in a random order using a custom-built olfactometer[72]. The odours (caproic acid and 1-hexanol) were randomly assigned as odour A or B for each mouse. Odour delivery lasted until mice left the centre port. Mice were required to stay in the centre odour port for >100 ms and to then choose the left or right water port depending on the identity of the presented odour. After poking into a correct water port, a drop of water (about 6 μl) was immediately delivered. The minimally allowed inter-trial interval (measured after water onset or after any type of error) was fixed to 4 s in the first 2 sessions, and then gradually increased by 1 s increments per session if the mouse completed >30 trials per session but did not improve in accuracy compared with previous sessions. The inter-trial interval was decreased if the mouse completed ≤30 trials or improved in accuracy. An odour port entry that occurred during the inter-trial interval was considered invalid and did not trigger an odour delivery. Mice often make a bout of multiple short pokes before triggering an odour delivery. The frequency of odours A and B was kept the same (50% each) in the first 2 sessions, and then adjusted to prevent a strong choice bias by increasing the frequency of the odour delivery that generated less reward (less than half of the other side) by 10% increments per session. Once the choice bias was eliminated, the odour frequency was changed back to 50% each. The odour port assignment (left or right) was held constant for each mouse. Mouse behaviour was monitored using infrared break-beam sensors attached to the centre odour port and the left and right water ports. Reaction time, movement time and trial completion time were quantified in the first two sessions of the odour discrimination task. The number of centre port pokes and trial initiation time were quantified during all of the sessions of the odour discrimination task. Reaction time was defined as the duration from odour delivery onset to when a mouse exited the odour port. Movement time was defined as the duration from when a mouse exited the odour port to when it entered a water port. Trial completion time was defined as the sum of reaction time and movement time. Trial initiation time was defined as the duration from the reward onset to the next entry to the odour port after successful trials, and from the water port entry to the next entry to the odour port after error trials. Trial initiation time was calculated using the first odour port entry regardless of whether it occurred during or after an inter-trial interval. Each session lasted for 1 h, and data were collected until each mouse achieved >90% accuracy in 2 consecutive sessions.

Probabilistic cue-reward association with fibre photometry in head-fixed mice

Photometry imaging in head-fixed mice was performed as previously established[12,73] with a custom-built fibre photometry system. Blue light (473 nm DPSS laser, Opto Engine) and green light (561 nm DPSS laser, Opto Engine) were filtered (4.0 optical density, Thorlabs) and coupled to an optical fibre patch cord (400 μm, Doric) using a 0.65 NA ×20 objective lens (Olympus). The patch cord was connected to the implanted

fibre to deliver excitation light and to collect fluorescence signals from the brain simultaneously. The detected fluorescence signals were converted to electrical signals using photodiodes (FDS10X10, Thorlabs). Electrical signals were amplified by current amplifiers (SR570, Stanford Research Systems) and collected by a multifunction I/O card (PCIe-6321, National Instruments) at 1,000 Hz. The light power was adjusted to a standard range for each sensor measured at the fibre end at multiple time points during the training period (473 nm: 90–100 μW for $GRAB_{DA}$; 561 nm: 80–90 μW for tdTomato). The mice recovered from surgery for 1 week, and were then water-restricted in the cages and hand-held for 10 min each on 3 days. During water restriction, the weight of each mouse was maintained above 85% of its initial body weight. The mice were then habituated to the experimental set up for 7–20 days; this included free water consumption from a tube and reliable water consumption during at least 68 free water trials per day when mice were head-fixed was used as a standard to start day 1 of the cue-reward association experiments. The mice were then trained with odour-based cue-reward association trials and unexpected free water trials for days 1–20 of the training phase. Mice were offered a constant volume (about 6 μl) of water in rewarded trials and in the free water trials. Each association trial began with an odour cue (for 1 s) delivered using a custom olfactometer[72], followed by a 2 s delay and then an outcome (water or no-water) was delivered. Each odour was dissolved in mineral oil at 1:10 dilution, and 30 μl of diluted odour solution was applied to the syringe filter (2.7 μm pore, 13 mm, Whatman, 6823-1327). Odorized air was further diluted in filtered air at 1:8 to produce air flow at 900 ml min^{-1} flow rate. Three chemicals, 1-butanol, caproic acid and isoamyl acetate, were used as odour cues and were randomized for association trial types across mice, but constant for the same mouse. Three association trial types were used: odour 1 predicting 100% chance of a water reward from day 1 to day 7 and an 80% chance from day 8 to day 20; odour 2 predicting a 40% chance of a water reward from day 1 to day 20; and odour 3 predicting 0% chance of a water reward from day 1 to day 20. Odour trials and free water trials were given in a block structure with each block containing 17 trials. Within each block, trials were pseudo-randomized, and free water trials accounted for 11.8% (2 out of 17 trials) of all trials, whereas odour trials constituted 29.4% (5 out of 17 trials) for each odour. A variable inter-trial interval drawn from an exponential distribution (10–20 s, average 13 s) was used between trials, resulting in a flat hazard function. On each day, mice were run through 6 blocks of 102 trials from day 1 to 7, and 10 blocks of 170 trials from day 8 to 20 or until they stopped collecting water through licking. Fibre photometry was used to record $GRAB_{DA}$ signals in ventral striatum on odd days (1, 3, … 19) and in the dorsal striatum on even days (2, 4, … 20). Trials were controlled through a NIDAQ board and were programmed using Labview. Licking from a waterspout was detected with a photoelectric sensor that generated a voltage change when the light path was blocked. The timing of each lick was detected at the peak of the voltage signal above a minimum and below a maximum threshold. Behaviour and photometry signals were analysed on each training day, and day 1 (early training) and day 17 (matured performance in RIM control mice) were used for display in figures and related statistical analyses. In all trials (odour trials and free water trials), the lick rate was calculated as the moving average over a 200-ms time window. In free water trials, the $GRAB_{DA}$ peak was calculated using the maximum value in a time window of 0.2–1.2 s after water delivery. Peak licks were calculated using the maximum lick rate within the first second of water delivery. Mean delayed licks were calculated using the average lick rate within 1–3 s after water delivery. In odour trials, anticipatory licks were defined as total licks during the 2 s delay period between odour cue delivery and the water/no-water delivery time point. Peak reward licks for odour trials were defined as peak licks within the first second of water delivery. Average $GRAB_{DA}$ responses in Fig. 5j–l and Extended Data Fig. 10m–q were calculated using the mean value within a defined time window for each condition (within 0–3 s after odour onset for odour response, within 0.2–1.2 s after outcome onset for reward responses, within 1.5–2.5 s after outcome onset for omission responses). To compare F_0, the raw photometry signal was processed with a low-pass filter at 0.01 Hz and the mean F_0 value of the time window from 40 s to 260 s of each recording session was calculated.

Statistics and reproducibility

Data are shown as the mean ± s.e.m. with $^*P < 0.05$, $^{**}P < 0.01$, $^{***}P < 0.001$. Data were collected using HCImage (v.4.2.6.1), Point Grey FlyCap (v.2.13.3.61), Bonito CL-400B/C, ThorCam (v.3.6.0.6), Matlab (v.R2020b) or Labview 2018, and analysed using Matlab (v.R2020b) or DeepLabCut (v.2.2). Data were plotted using Matlab (MathWorks) and/or Prism (GraphPad). Sample sizes for each plot are provided in each figure legend; sample sizes were determined based on previous studies and are similar to studies published in the field[12,30,46,60,74]. Because of limited sample size and frequent non-Gaussian data distributions, non-parametric tests were used for statistical analyses whenever possible. For two-group comparisons, two-sided Mann–Whitney rank-sum tests were used for slice $GRAB_{DA}$ imaging, slice amperometry, gait analyses, horizontal bar tests, vertical bar tests, movement before and after drug infusions in the dorsal striatum, analyses of movement and photometry data in open-field arenas ($\Delta F/F_0$ variation of s.d. of $GRAB_{DA}$ and GCaMP6s; cross-correlation of GCaMP6s and RdLight1 in a time window of −200 ms to 200 ms; F_0 of $GRAB_{DA}$, GCaMP6s, RdLight1 and tdTomato; peak $GRAB_{DA}$; peak velocity of movement initiations), centre entry speed in food-CPP, two odour discrimination tasks, and analyses of licks and $GRAB_{DA}$ data on days 1 and 17 of cue-reward association experiments. For comparisons of more than two groups, Kruskal–Wallis analysis of variance was used for distance travelled in baseline and reserpine plus L-DOPA compared with reserpine, $GRAB_{DA}$ $\Delta F/F_0$ variation in reserpine or reserpine plus L-DOPA experiments, and F_0 of $GRAB_{DA}$ and tdTomato. Repeated measures two-way ANOVA tests (sphericity not assumed, Geisser–Greenhouse correction) were used for rotarod experiments, movement initiation frequency analyses, time in the food-associated chamber and centre crossing frequency in food-CPP, and anticipatory licks in cue-reward associations. Two-way ANOVA was used for apomorphine-induced rotations after 6-OHDA dopamine denervation. In photometry experiments, the tdTomato signal was acquired for visual exclusion of movement artefacts, but the signal was not included for statistical comparisons. The specific statistical tests used are described in each figure legend, *P* value ranges are shown in each figure and exact *P* values are tabulated in Supplementary Table 1.

Reporting summary

Further information on research design is available in the Nature Portfolio Reporting Summary linked to this article.

Data availability

Data points generated for this study are included in the figures whenever possible. Tabulated data for all figures are available at Zenodo (https://doi.org/10.5281/zenodo.13329864)[75]. Additional data are available from the corresponding author upon request.

61. Kaeser, P. S. et al. RIM1α and RIM1β are synthesized from distinct promoters of the *RIM1* gene to mediate differential but overlapping synaptic functions. *J. Neurosci.* **28**, 13435–13447 (2008).
62. Kaeser, P. S. et al. RIM proteins tether Ca^{2+} channels to presynaptic active zones via a direct PDZ-domain interaction. *Cell* **144**, 282–295 (2011).
63. Zhou, Q. et al. Architecture of the synaptotagmin–SNARE machinery for neuronal exocytosis. *Nature* **525**, 62–67 (2015).
64. Backman, C. M. et al. Characterization of a mouse strain expressing Cre recombinase from the 3′ untranslated region of the dopamine transporter locus. *Genesis* **44**, 383–390 (2006).
65. *Allen Mouse Brain Atlas [mouse, P56, coronal 2011]* (Allen Institute for Brain Science, 2004); https://atlas.brain-map.org.

66. Chen, T.-W. et al. Ultrasensitive fluorescent proteins for imaging neuronal activity. *Nature* **499**, 295–300 (2013).
67. Rudolph, S. et al. Cerebellum-specific deletion of the $GABA_A$ receptor δ subunit leads to sex-specific disruption of behavior. *Cell Rep.* **33**, 108338 (2020).
68. Newell, A., Yang, K. & Deng, J. Stacked hourglass networks for human pose estimation. In *Computer Vision—ECCV 2016. Lecture Notes in Computer Science* vol. 9912 (eds Leibe, B., Matas, J., Sebe, N. & Welling, M.) 484–499 (Springer, 2016).
69. Mathis, A. et al. DeepLabCut: markerless pose estimation of user-defined body parts with deep learning. *Nat. Neurosci.* **21**, 1281–1289 (2018).
70. Nath, T. et al. Using DeepLabCut for 3D markerless pose estimation across species and behaviors. *Nat. Protoc.* **14**, 2152–2176 (2019).
71. Hutchison, M. A. et al. Genetic inhibition of neurotransmission reveals role of glutamatergic input to dopamine neurons in high-effort behavior. *Mol. Psychiatry* **23**, 1213–1225 (2018).
72. Uchida, N. & Mainen, Z. F. Speed and accuracy of olfactory discrimination in the rat. *Nat. Neurosci.* **6**, 1224–1229 (2003).
73. Menegas, W. et al. Dopamine neurons projecting to the posterior striatum form an anatomically distinct subclass. *eLife* **4**, e10032 (2015).
74. Nguyen, N. D. et al. Cortical reactivations predict future sensory responses. *Nature* **625**, 110–118 (2024).
75. Cai, X. & Kaeser, P. Data table for Cai et al., 2024. *Zenodo* https://doi.org/10.5281/zenodo.13329864 (2024).
76. Brimblecombe, K. R., Gracie, C. J., Platt, N. J. & Cragg, S. J. Gating of dopamine transmission by calcium and axonal N-, Q-, T- and L-type voltage-gated calcium channels differs between striatal domains. *J. Physiol.* **593**, 929–946 (2015).
77. Tedford, H. W. & Zamponi, G. W. Direct G protein modulation of Ca_v2 calcium channels. *Pharmacol. Rev.* **58**, 837–862 (2006).
78. Pereira, D. B. et al. Fluorescent false neurotransmitter reveals functionally silent dopamine vesicle clusters in the striatum. *Nat. Neurosci.* **19**, 578–586 (2016).
79. Delignat-Lavaud, B. et al. Synaptotagmin-1-dependent phasic axonal dopamine release is dispensable for basic motor behaviors in mice. *Nat. Commun.* **14**, 4120 (2023).
80. Kaeser, P. S. & Regehr, W. G. Molecular mechanisms for synchronous, asynchronous, and spontaneous neurotransmitter release. *Annu. Rev. Physiol.* **76**, 333–363 (2014).

Acknowledgements This work was supported by the NIH (R01NS103484 and R01DA056109 to P.S.K., R01DA058777 to P.S.K. and N.U., R01NS108740 and U19NS113201 to N.U., R01MH125162 to M.W.-U.), the Dean's Initiative Award for Innovation (to P.S.K.), and a Harvard-MIT Joint Research Grant (to P.S.K. and N.U.). We thank C. Qiao, J. Wang, V. Charles and G. Handy for assistance with mouse genetic experiments; I. Quintus-Bosz for help with acquisition of gait data; and R. Wise, S. R. Datta, B. Sabatini, C. Harvey, V. Murthy, J. Assad, W. Regehr and J. Williams for discussions and/or comments on the manuscript. X.C. initially received a PhD Mobility National Grants fellowship from Xi'an Jiaotong University/China Scholarship Council for a visiting graduate studentship. X.C. is currently at the Beth Israel Deaconess Medical Center. C.L. is currently at Westlake University. I.T.-K. is currently at Keio University. C.G. was supported by a Stuart H.Q. & Victoria Quan Fellowship and is currently at Flagship Pioneering. A.B. is a recipient of a Brain and Behavior Research Foundation Young Investigator Grant (#31271). R.A. is a recipient of a Harvard Brain Initiative Postdoc Pioneers Grant. Y.X. was a visiting undergraduate student from the University of Science and Technology of China and is currently at the Department of Brain and Cognitive Sciences at MIT.

Author contributions Conceptualization: X.C., C.L., M.W.-U., N.U. and P.S.K. Methodology: X.C., C.L., I.T.-K., J.-H.L., C.G., R.A., Y.X. and M.W.-U. Formal analyses: X.C., C.L., I.T.-K., J.-H.L., C.G., M.W.-U., N.U. and P.S.K. Investigation: X.C., C.L., I.T.-K., C.G., A.B., J.L. and M.W.-U. Resources: X.C., C.L., J.-H.L., C.G., A.B., T.P. and Y.L. Writing original draft: X.C., C.L. and P.S.K. Writing, reviewing and editing: X.C., C.L., I.T.-K., J.-H.L., C.G., A.B., J.L., R.A., Y.X., T.P., Y.L., M.W.-U., N.U. and P.S.K. Funding acquisition: N.U. and P.S.K. Detailed experimental contributions are as follows: X.C., Fig. 1k–o, p–t (with help from C.L.), Figs. 2, 3, 4a–e and 5 (with help from R.A.) and Extended Data Figs. 1u–af, 2–5, 6d–i, 7–9 and 10e–s (with help from R.A.); C.L., Fig. 1a–d; A.B., Extended Data Figs. 1a–i and 10a–d; C.G., Fig. 1e–j and Extended Data Fig. 1j–t; J.L., Extended Data Fig. 6a–c (with help from X.C.); I.T.-K. and M.W.-U., Fig. 4f–m.

Competing interests Y.L. is listed as an inventor on a patent application (PCT/CN2018/107533) describing GRAB probes. T.P. is listed as an inventor on a patent application (PCT/US2017/062993) describing the RdLight1 probe. The other authors declare no competing interests.

Additional information
Supplementary information The online version contains supplementary material available at https://doi.org/10.1038/s41586-024-08038-z.
Correspondence and requests for materials should be addressed to Pascal S. Kaeser.
Peer review information *Nature* thanks Patricia Janak and the other, anonymous, reviewer(s) for their contribution to the peer review of this work.

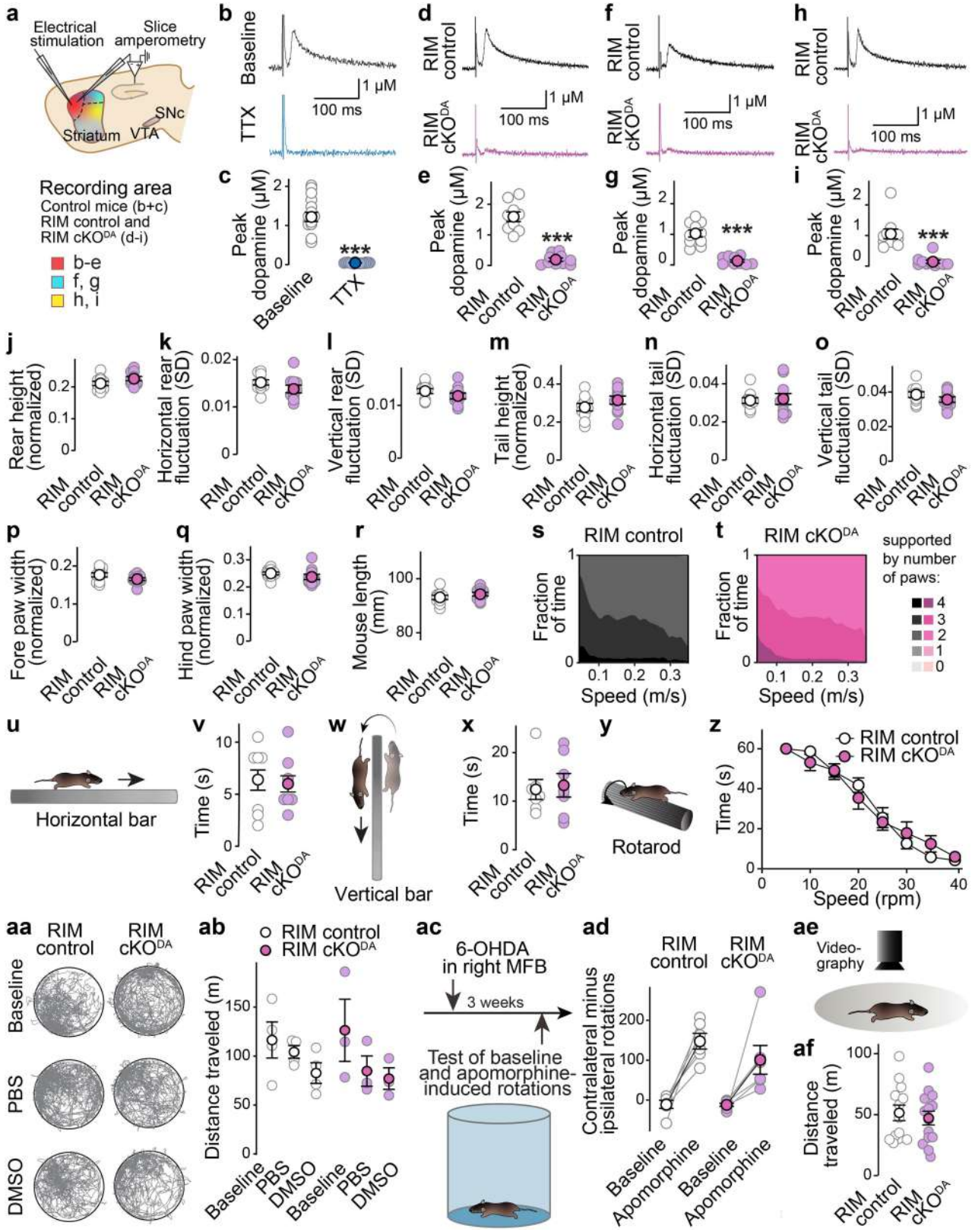

Extended Data Fig. 1 | See next page for caption.

Extended Data Fig. 1 | Slice amperometry in dorsal striatum and additional movement analyses of RIM cKO^{DA} mice. a, Schematic of slice amperometry in subareas of the dorsal striatum. **b**,**c**, Example traces (**b**) and quantification (**c**) of peak amplitudes of dopamine release evoked by electrical stimulation before and after 1 µM tetrodotoxin (TTX), 16 slices from 4 mice. **d**,**e**, Example traces (**d**) and quantification (**e**) of peak amplitudes as in **b** and **c**, RIM control 9 slices from 4 mice, RIM cKO^{DA} 10/4. **f**–**i**, As **d**,**e**, but in the other subareas shown in **a**, RIM control 10/4, RIM cKO^{DA} 10/4. **j**–**t**, Quantification of parameters of gait, RIM control 1122 cycles from 10 mice, RIM cKO^{DA} 1206/10. **u**–**z**, Schematics (**u**,**w**,**y**) and analyses (**v**,**x**,z) of horizontal bar, vertical bar and rotarod (after four days of training) tests, RIM control 7 mice, RIM cKO^{DA} 7. **aa**,**ab**, Representative trajectories (**aa**) and quantification of distance travelled in 30 min (**ab**) before (day 1) and after i.p. injection of PBS (day 2) and DMSO (day 4), RIM control 4, RIM cKO^{DA} 3. **ac**,**ad**, Schematic (**ac**) of unilateral 6-OHDA lesions followed by analyses of rotations before and after i.p. injection of the D1 and D2 receptor agonist apomorphine in 6-OHDA pre-treated mice (1 mg/kg) and quantification of net contralateral rotations (**ad**), RIM control 6, RIM cKO^{DA} 6. **ae**,**af**, Schematic of videography (**ae**) and analyses of distance travelled in 30 min (**af**) for the mice in Fig. 1p–t, RIM control 13, RIM cKO^{DA} 14. Some of the data are from the baseline condition shown in Fig. 1m and these data points are replotted here. Data are mean ± SEM; *** $p < 0.001$, assessed by: two-sided Mann-Whitney rank-sum tests for **c**, **e**, **g**, **i**, **j**–**r**, **v**, **x**, **af**; two-way ANOVA for **z**, **ad**; and Kruskal-Wallis analysis of variance with post-hoc Dunn's tests for **ab**. For videos of gait, see Supplementary Video 1.

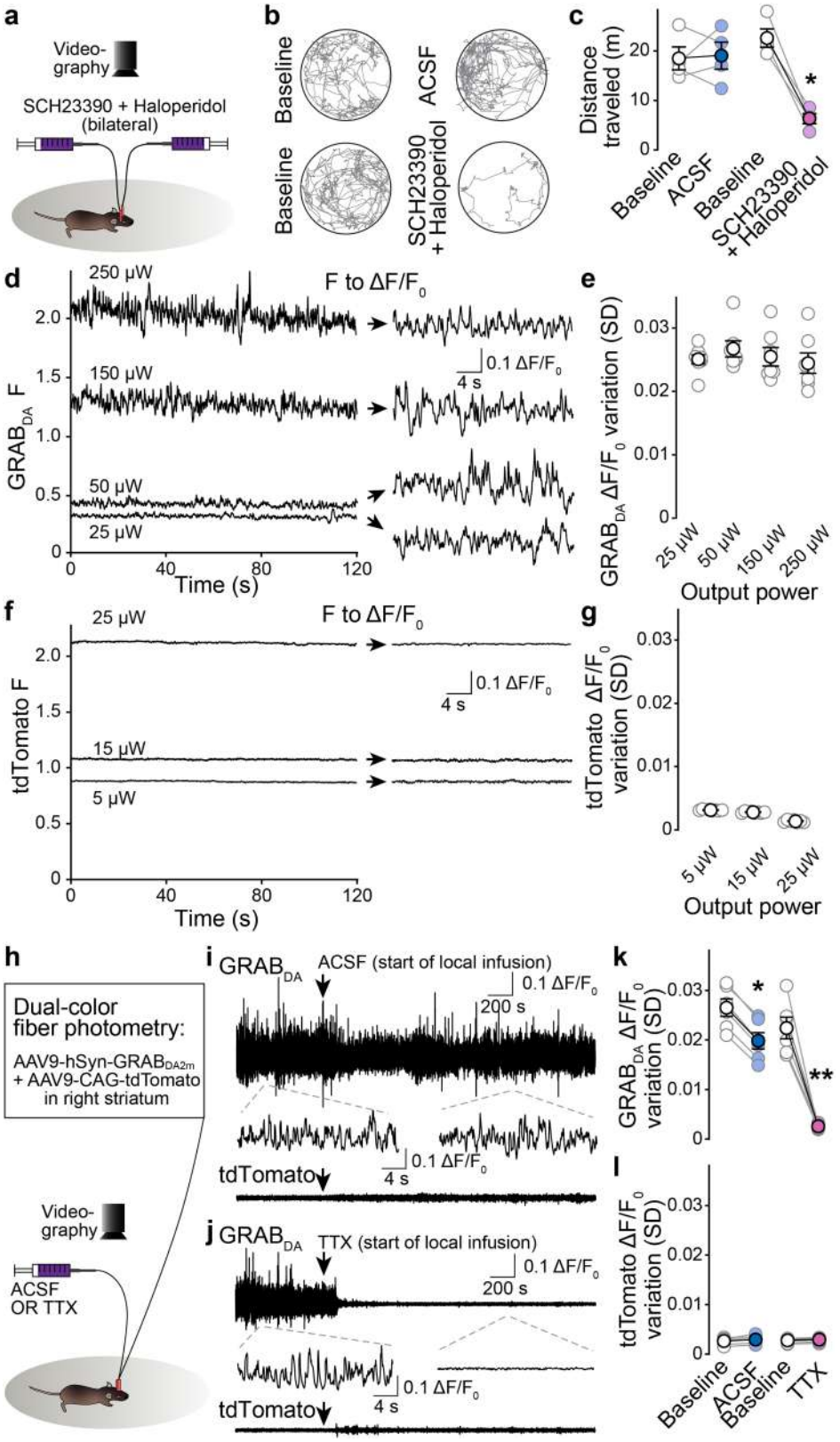

Extended Data Fig. 2 | See next page for caption.

Extended Data Fig. 2 | Pharmacological inhibition of locomotion by drug infusion and assessment of excitation power output. a, Schematic of assessment of movement with bilateral drug infusion in dorsal striatum. **b**,**c**, Representative trajectories (**b**) and quantification of total distance traveled in 15 min (**c**) before and after local infusion of ACSF or D1 (SCH23390, 20 μM, 1 μl for each site) and D2 (haloperidol, 40 μM, 1 μl for each site) receptor antagonists, 4 mice. **d**,**e**, Example traces (**d**) and quantification (**e**) of fluorescence variation quantified as standard deviation (SD) of $\Delta F/F_0$ of $GRAB_{DA}$ fluorescence at variable output power in freely moving mice, 7 mice. **f**, **g**, As in **d**,**e**, but for tdTomato, 7 mice; **d**–**g** reveal that $\Delta F/F_0$ variation is similar across excitation output powers. **h**, Schematic of the measurement of dopamine dynamics in freely moving mice. Fibre photometry and drug delivery were in the right dorsal striatum with an optofluid cannula. **i**–**l**, Example traces (**i**,**j**) and quantification of the variation of $\Delta F/F_0$ of $GRAB_{DA}$ (**k**) and of tdTomato (**l**) fluorescence before and after local infusion of the sodium channel blocker TTX (500 nM, 1 μl), 6 mice. Data are mean ± SEM; * $p < 0.05$, ** $p < 0.01$, assessed by two-sided Mann-Whitney rank-sum tests for **c**, **k**; Kruskal-Wallis analysis of variance with post-hoc Dunn's tests were used for **e**, **g**.

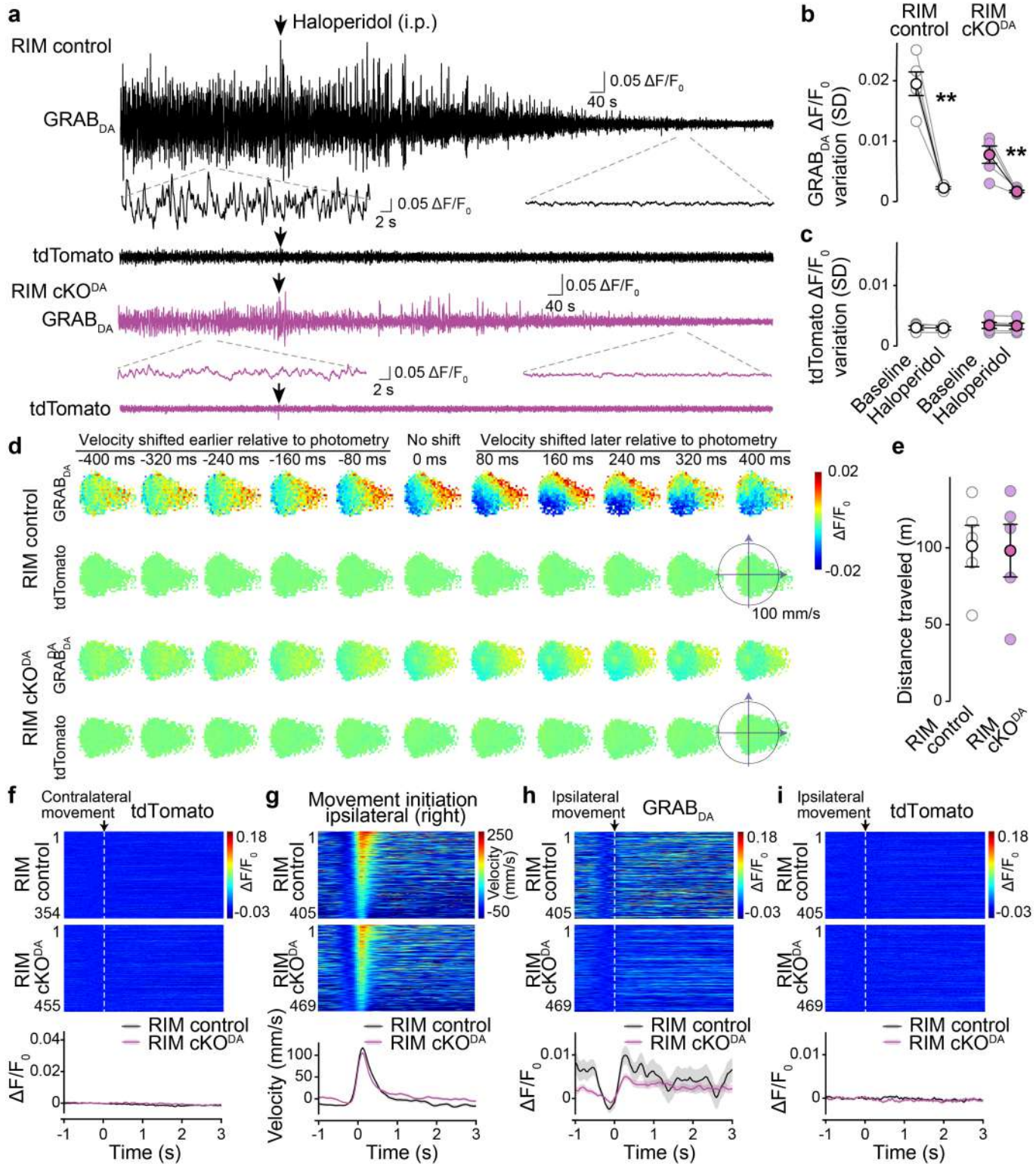

Extended Data Fig. 3 | Haloperidol injection and additional analyses of GRAB$_{DA}$ dynamics in RIM cKO^{DA} mice. a–c, Example traces (**a**) and quantification of the variation of $\Delta F/F_0$ of GRAB$_{DA}$ (**b**) and of tdTomato (**c**) fluorescence before and after i.p. injection of the D2 receptor antagonist haloperidol (2 mg/kg), RIM control 5 mice, RIM cKO^{DA} 5. **d**, Average GRAB$_{DA}$ and tdTomato signals registered to the artificially shifted instantaneous velocity plotted in polar coordinates for the experiment shown in Fig. 2g,h. The shifting of the velocity time course to earlier or later time points relative to the photometry illustrates that the GRAB$_{DA}$ fluorescence signal peaks after the velocity and suggests that dopamine signalling tracks the velocity time course, RIM control 5, RIM cKO^{DA} 5. **e**, Analyses of distance traveled for the experiment shown in Fig. 2, n as in **a**–**c**. **f**, Quantification of tdTomato fluorescence during contralateral movement initiations shown in Fig. 2i,j, event heatmaps are sorted by the order of the corresponding velocity signals in Fig. 2i, RIM control 354 events from 5 mice, RIM cKO^{DA} 455/5. **g**–**i**, Quantification of time courses of velocity amplitudes (**g**), and of GRAB$_{DA}$ (**h**) and tdTomato (**i**) fluorescence changes during ipsilateral movement initiations (right turns, velocity angles between 180° and 360°). Event heatmaps were sorted by the peak velocity amplitude in **g**, RIM control 405/5, RIM cKO^{DA} 469/5. Data are mean ± SEM; ** $p < 0.01$, assessed by two-sided Mann-Whitney rank-sum tests for **b**, **e**.

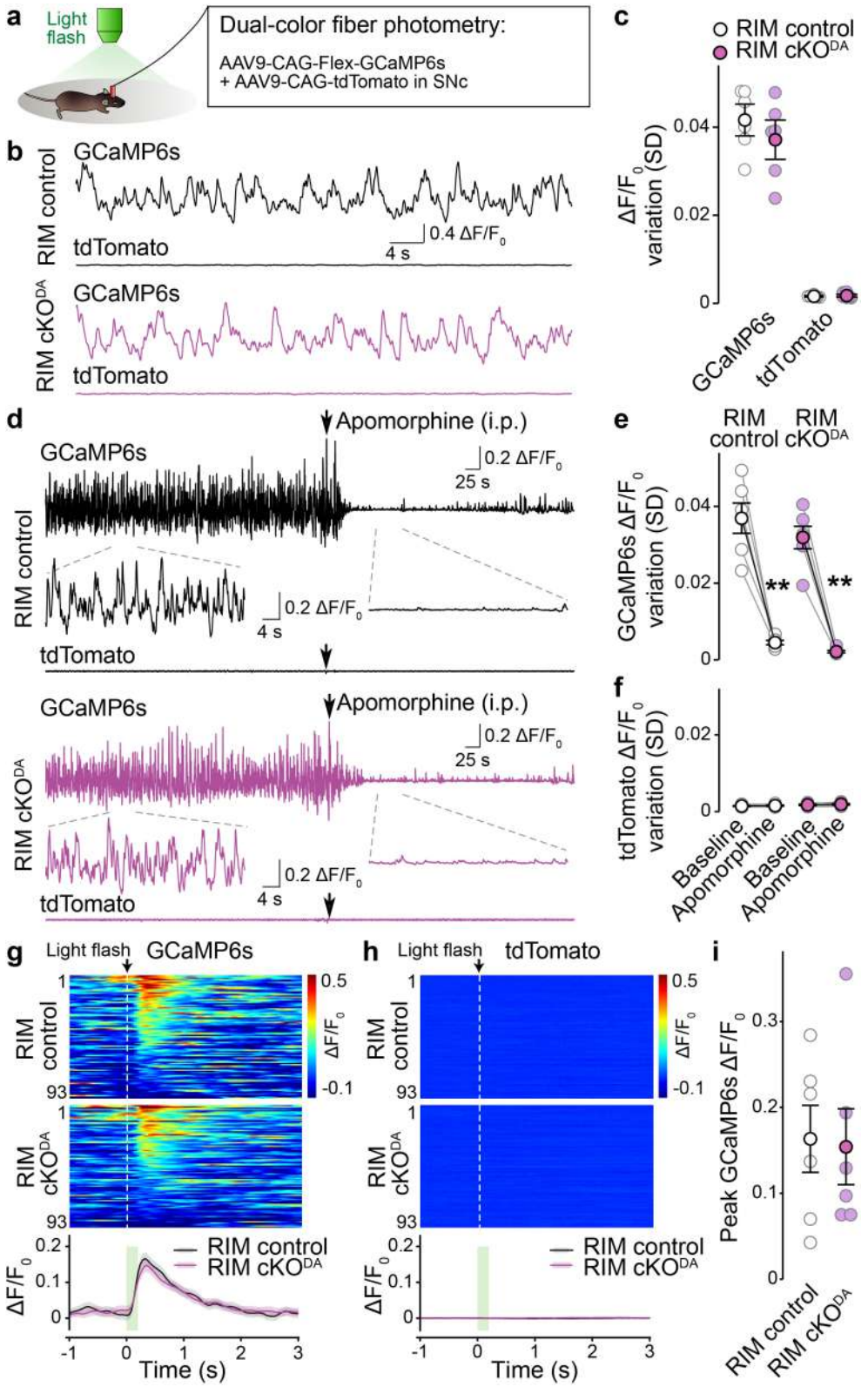

Extended Data Fig. 4 | See next page for caption.

Extended Data Fig. 4 | In vivo GCaMP6s fluctuations in RIM cKO^{DA} mice. **a**, Strategy for dual-colour fibre photometry of dopamine axonal GCaMP6s and tdTomato. **b**,**c**, Example traces (**b**) and quantification (**c**) of fluorescence variation as SD of $\Delta F/F_0$ of GCaMP6s and of tdTomato in freely moving mice, RIM control 6 mice, RIM cKO^{DA} 6. **d**–**f**, Example traces (**d**) and quantification of fluorescence variation as SD of $\Delta F/F_0$ of GCaMP6s (**e**) and of tdTomato (**f**) before and after i.p. injection of the D1 and D2 receptor agonist apomorphine (1 mg/kg). The suppression of GCaMP6s fluorescence changes by apomorphine indicates that GCaMP6s fluorescence changes reflect activity-dependent depolarizations of dopamine axons that are inhibited by D2 auto-receptors, n as in **b**,**c**. **g**–**i**, Time course of fluorescence in individual trials (event heatmaps, top) and average data (bottom) for GCaMP6s (**g**) and tdTomato (**h**) fluorescence aligned to the sensory stimulation (dashed line), and peak GCaMP6s per mouse (**i**). Event heatmaps in **g**,**h** were sorted by the peak amplitude in **g**, RIM control 93 events from 6 mice, RIM cKO^{DA} 93/6. The finding that axonal Ca^{2+} dynamics are not detectably changed in RIM cKO^{DA} mice is unexpected given RIMs role in targeting Ca_V2 channels to presynaptic active zones[62]. It could be due to distinct RIM functions in dopamine neuron axons[34,62], due to a distinct set of Ca^{2+} channels in dopamine axons[30,76], due to compensatory effects in RIM cKO^{DA} mice because of loss of the D2 auto-receptor feedback[77], due to technical differences in experiments, or due to Ca^{2+} entry away from active zones[78] and not under the control of RIM, which might be enhanced if Ca_V2 channels are mislocalized. Data are mean ± SEM; ** $p < 0.01$, assessed by two-sided Mann-Whitney rank-sum tests for **c**, **e**, **i**.

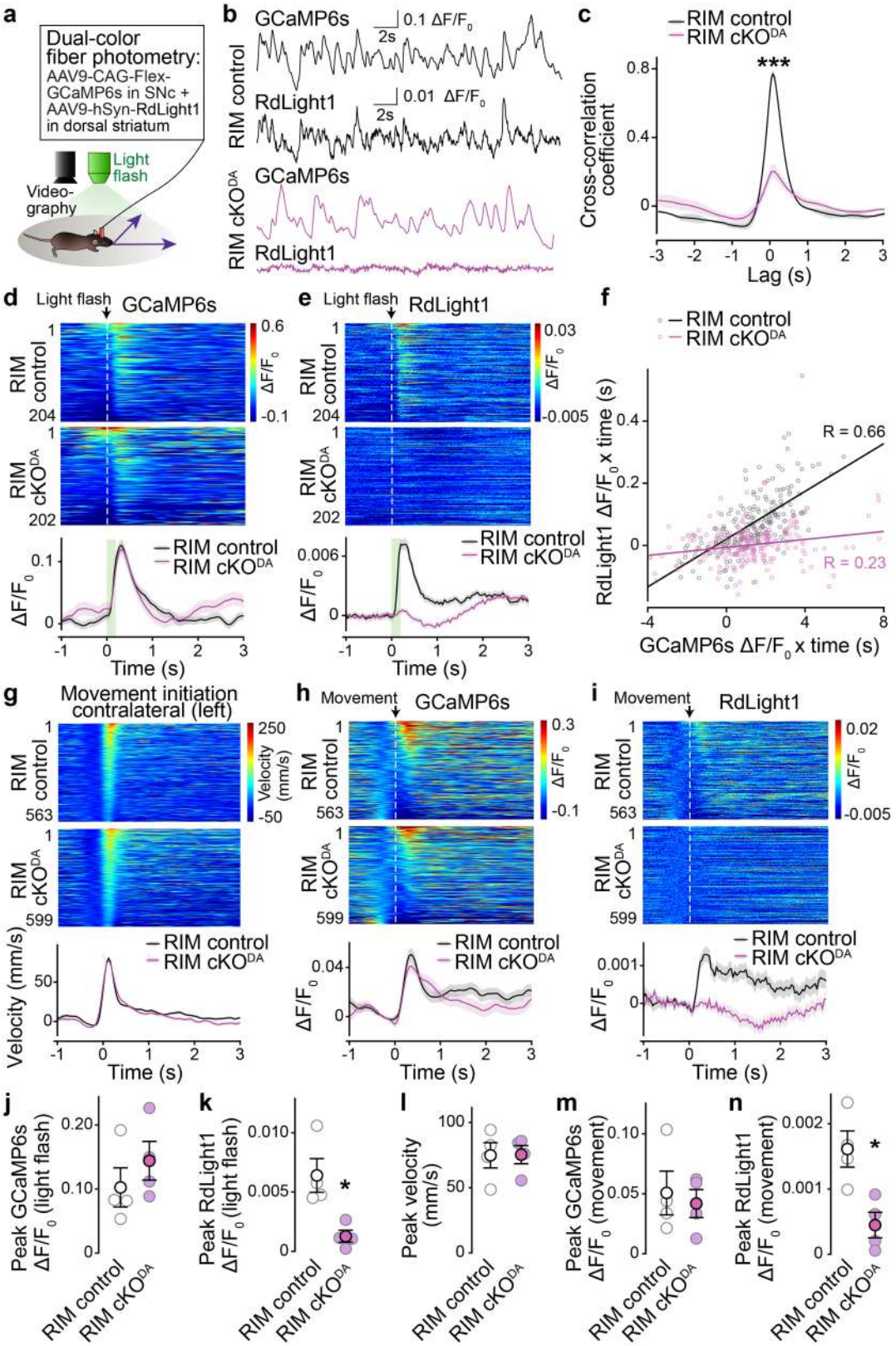

Extended Data Fig. 5 | See next page for caption.

Extended Data Fig. 5 | Assessment of dopamine axon GCaMP6s and striatal RdLight1 dynamics in RIM cKO^{DA} mice. a, Schematic for assessment of fluorescence of GCaMP6s expressed in striatal dopamine axons and RdLight1 expressed in striatal neurons. **b**,**c**, Example traces (**b**) and cross-correlation (**c**) of GCaMP6s and RdLight1 signals, RIM control 4 mice, RIM cKO^{DA} 4. **d**,**e**, Individual (event heatmaps, top) and average (bottom) time courses of GCaMP6s (**d**) and RdLight1 (**e**) fluorescence aligned to the light flash (dashed line). Event heatmaps in **d**,**e** were sorted by the peak amplitude in d, RIM control 204 events from 4 mice, RIM cKO^{DA} 202/4. **f**, Correlation analyses of transients in **d**,**e** (area under the curve, 0 to 600 ms after stimulation), RIM control 203/4, RIM cKO^{DA} 198/4. **g**–**i**, Individual (event heatmaps, top) and average (bottom) time courses of velocity amplitudes (**g**), and of GCaMP6s (**h**) and RdLight1 (**i**) fluorescence during contralateral movement initiations. Event heatmaps in **g** were sorted by the peak velocity amplitude, and in **h**,**i** by the peak amplitude of GCaMP6s in h, RIM control 563/4, RIM cKO^{DA} 599/4. **j**–**n**, Analyses of peaks from **d**,**e**, and **g**–**i** for each mouse, n as in **b**,**c**. There was a strong positive correlation in RIM control mice between GCaMP6s and RdLight1 fluctuations that was disrupted in RIM cKO^{DA} mice (**c**). Field illuminations induced dopamine axonal GCaMP6s transients in both genotypes, but failed to trigger dopamine release in RIM cKO^{DA} mice (**d**–**f**). Axonal Ca^{2+} dynamics and striatal dopamine fluctuations correlated during contralateral turns in RIM control mice. In RIM cKO^{DA} mice, only Ca^{2+} transients, not movement-associated dopamine transients, were detected (**g**–**i**). Together with Extended Data Fig. 4, the data suggest that dopamine neuron firing and the underlying regulatory network are not strongly disrupted in RIM cKO^{DA} mice. Data are mean ± SEM; * $p < 0.05$, *** $p < 0.001$, assessed by: two-sided Mann-Whitney rank-sum tests for areas under the curve in **c**,**j**–**n**.

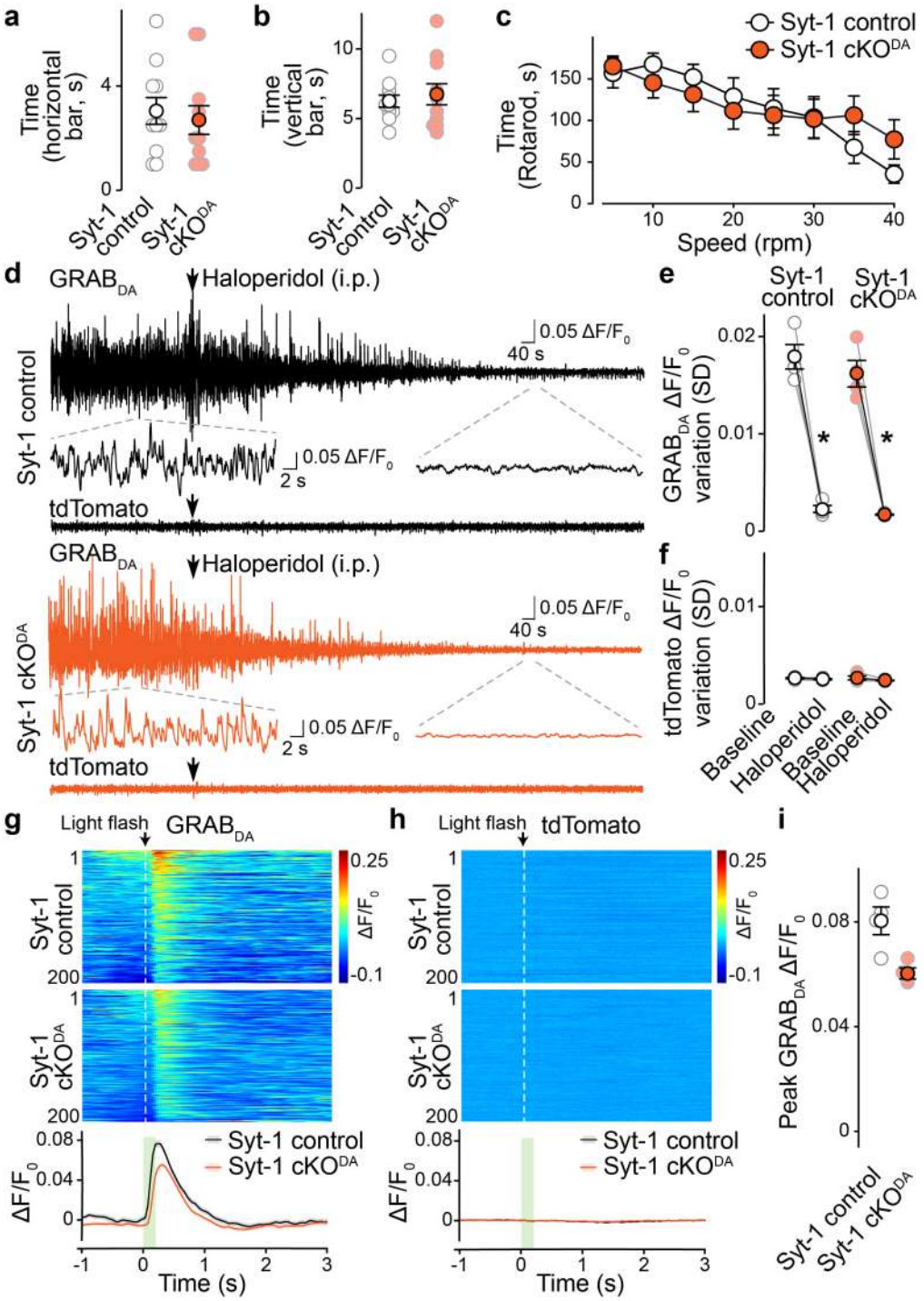

Extended Data Fig. 6 | Ablating the Ca^{2+} sensor Syt-1 in dopamine neurons does not disrupt in vivo dopamine dynamics or locomotor behaviors. **a**–**c**, Analyses of motor behaviours as in Extended Data Fig. 1u–z, but for Syt-1 control and Syt-1 cKO^{DA} mice. For dopamine release analyses in Syt-1 cKO^{DA}, see[41]. The time spent to cross a horizontal bar (**a**), to climb down a vertical bar (**b**), or the latency to fall from a rotarod after four days of training (**c**) are quantified, Syt-1 control 10 mice, Syt-1 cKO^{DA} 10. **d**–**i**, In vivo fibre photometry performed as in Fig. 2 and Extended Data Fig. 3, but for Syt-1 cKO^{DA} mice with example traces (**d**) and quantification of variation of $\Delta F/F_0$ of $GRAB_{DA}$ (**e**) and of tdTomato (**f**) fluorescence before and after i.p. injection of the D2 receptor antagonist haloperidol (2 mg/kg), and with individual (event heatmaps, top) and average (bottom) time courses of $GRAB_{DA}$ (**g**) and tdTomato (**h**) fluorescence aligned to the sensory stimulation (dashed line) and peak $GRAB_{DA}$ per mouse (**i**). Event heatmaps are sorted by the peak $GRAB_{DA}$ amplitude in **g**; Syt-1 control 200 events from 4 mice, Syt-1 cKO^{DA} 200/4. Altogether, knockout of Syt-1 from dopamine neurons did not disrupt motor function. Despite the strong impairment in dopamine release in brain slices[41,79], in vivo dopamine fluctuations were maintained, likely due to the remaining release after Syt-1 knockout, presumably asynchronous release[80], that is detected with in vivo microdialysis or in brain slices after dopamine transporter (DAT) blockade (striatum)[41], or in response to stimulus trains (somatodendritic release)[44]. Hence, removing the fast Ca^{2+} sensor from dopamine neurons does not suffice to abolish in vivo dopamine dynamics and Syt-1 cKO^{DA} mice cannot be used to test behavioural roles of these dynamics. Data are mean ± SEM; * $p < 0.05$, assessed by: two-sided Mann-Whitney rank-sum test for **a**, **b**, **e**, **i**; two-way ANOVA for **c**.

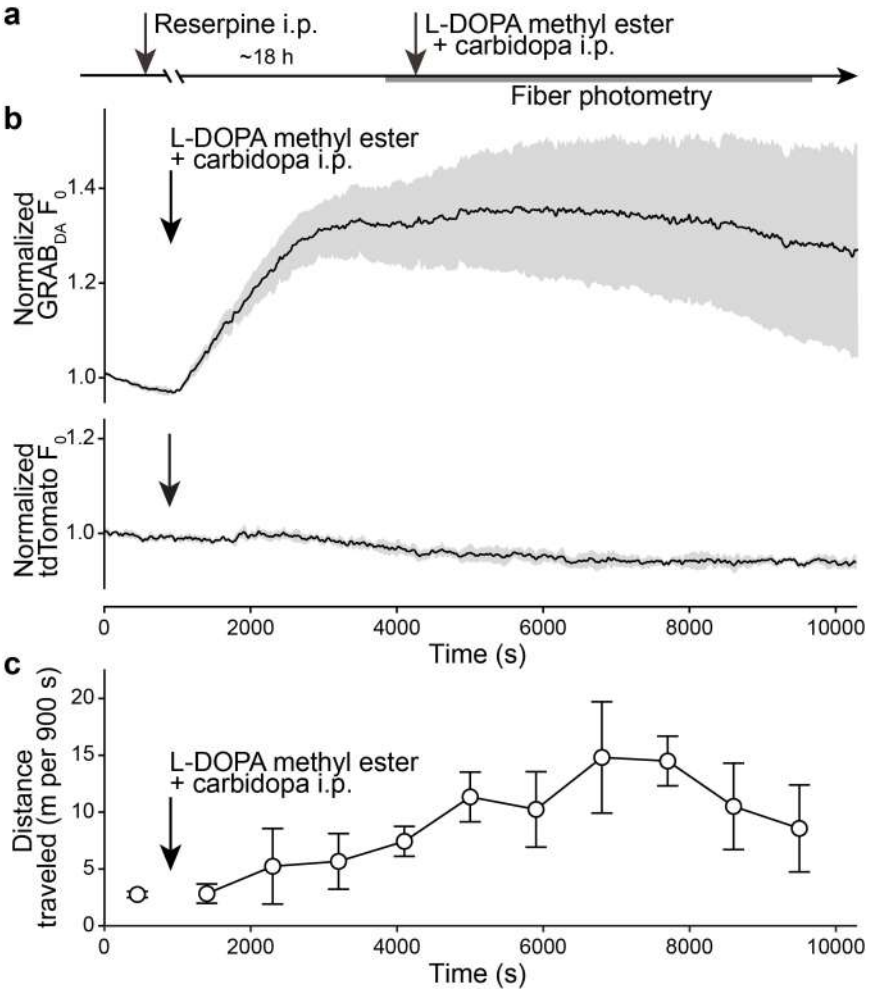

Extended Data Fig. 7 | Analyses of GRAB$_{DA}$ F$_0$ and locomotion after L-DOPA treatment in reserpine-depleted mice. a, Schematic of the experiment. **b**,**c**, Assessment of GRAB$_{DA}$ F$_0$ (**b**) and quantification of distance traveled (**c**, analysed in 900 s bins for the first 900 s and from 950–9950 s) before and after i.p. injection of L-DOPA (250 mg/kg L-dopa methyl ester with 25 mg/kg carbidopa) in mice treated with reserpine (3 mg/kg reserpine) ~18 h before L-DOPA injection, GRAB$_{DA}$ F$_0$ is normalized to the first 5 min, 3 mice. Data are mean ± SEM.

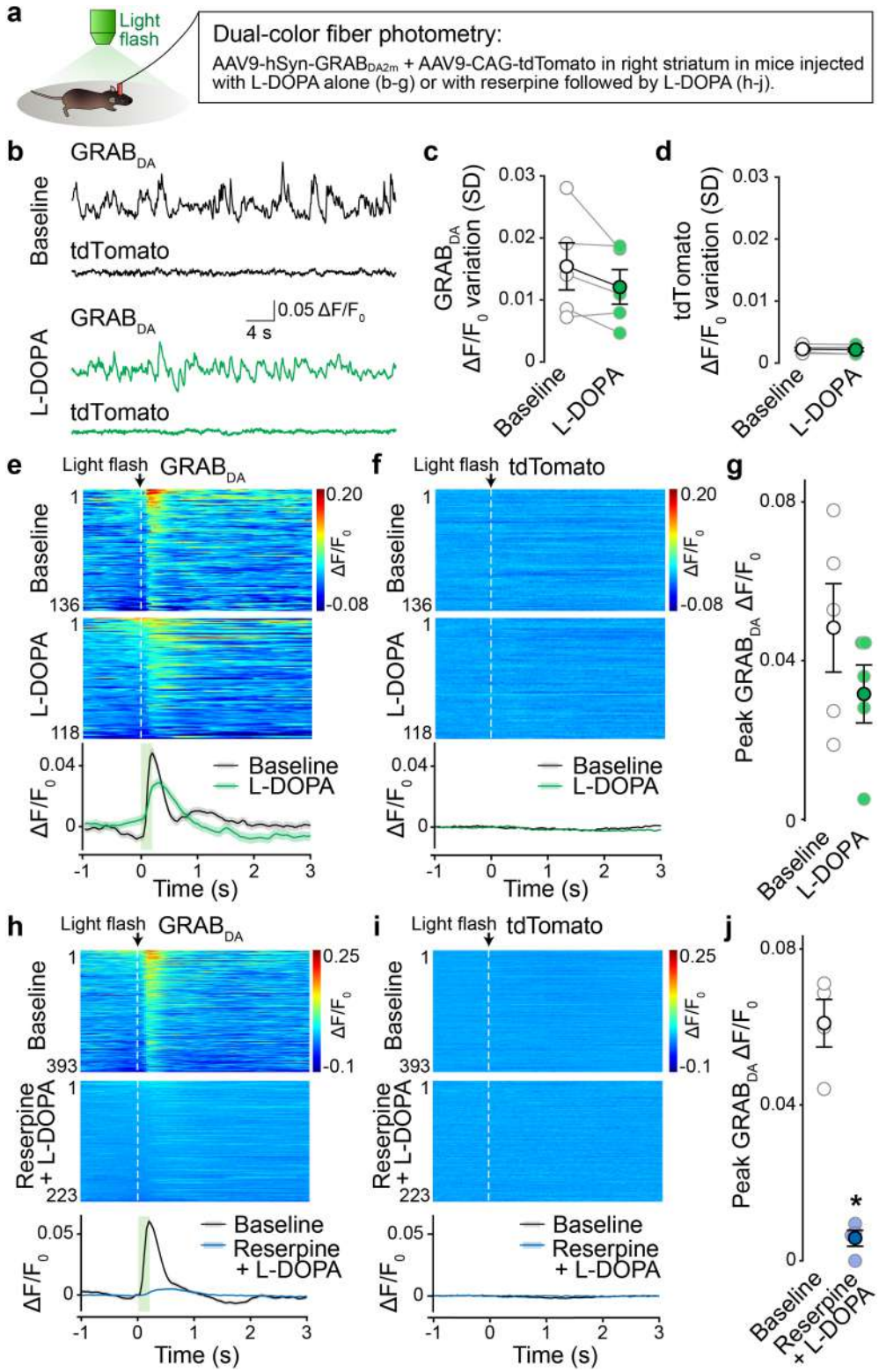

Extended Data Fig. 8 | Additional analyses L-DOPA treated mice. **a**, Schematic of the experiment. **b**–**d**, Example traces (**b**) and quantification of the variation of $\Delta F/F_0$ of $GRAB_{DA}$ (**c**) and of tdTomato (**d**) fluorescence before and after i.p. injection of L-DOPA (250 mg/kg L-dopa methyl ester with 25 mg/kg carbidopa), 5 mice. **e**–**g**, Individual (event heatmaps, top) and average (bottom) time courses of $GRAB_{DA}$ (**e**) and tdTomato (**f**) fluorescence aligned to the sensory stimulation (dashed line), and peak $GRAB_{DA}$ (**g**) for each mouse, before and after i.p. injection of L-DOPA. Data in **a**–**g** establish that $GRAB_{DA}$ fluorescence increases can be detected when L-DOPA is present without reserpine depletion, indicating that $GRAB_{DA}$ fluorescence is not saturated after L-DOPA injection. Event heatmaps in **e**,**f** were sorted by the peak $GRAB_{DA}$ amplitude in **e**, baseline 136 events from 5 mice, L-DOPA 118/5. **h**–**j**, Individual (event heatmaps, top) and average (bottom) time courses of $GRAB_{DA}$ (**h**) and tdTomato (**i**) fluorescence aligned to the sensory stimulation (dashed line), and peak $GRAB_{DA}$ (**j**) for each mouse, before and after i.p. injection of reserpine (3 mg/kg) and L-DOPA (250 mg/kg L-dopa methyl ester with 25 mg/kg carbidopa). Data were recorded during the experiment that is shown in Fig. 3b–j. Event heatmaps in **h**,**i** were sorted by the $GRAB_{DA}$ peak amplitude in **h**, baseline 393/4, reserpine + L-DOPA 223/4. Data are mean ± SEM; * $p < 0.05$, assessed by two-sided Mann-Whitney rank-sum tests in **c**, **g**, **j**.

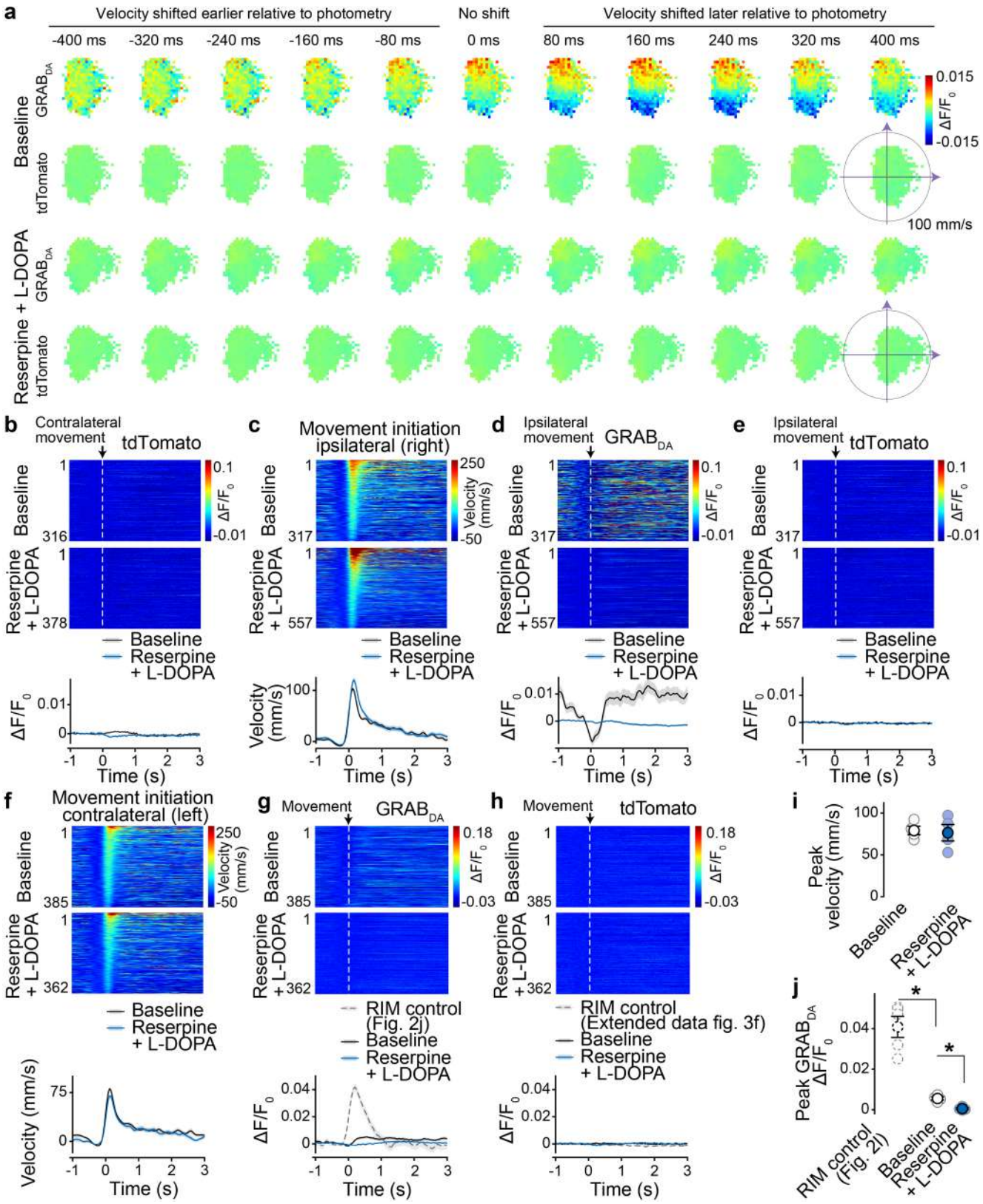

Extended Data Fig. 9 | See next page for caption.

Extended Data Fig. 9 | Additional analyses of $GRAB_{DA}$ fluorescence during movement initiation in reserpine and L-DOPA treated mice. a, Average $GRAB_{DA}$ and tdTomato signals registered to the artificially shifted instantaneous velocity plotted in polar coordinates before and after i.p. injection of reserpine (3 mg/kg) and L-DOPA (250 mg/kg L-dopa methyl ester with 25 mg/kg carbidopa) for the experiment shown in Fig. 3b-j, 4 mice. **b**, Quantification of tdTomato fluorescence during contralateral movement initiations shown in Fig. 3g,h, event heatmaps are sorted by the order of the corresponding velocity signals in Fig. 3g, baseline 316 events from 4 mice, reserpine + L-DOPA 378/4. **c**–**e**, Individual (event heatmaps, top) and average (bottom) time courses of velocity amplitudes (**c**) and $GRAB_{DA}$ (**d**) and tdTomato (**e**) fluorescence changes during ipsilateral movement initiations (right turns, velocity angles between 180° and 360°) for the experiment shown in Fig. 3b–j. Event heatmaps in **c**–**e** were sorted by the peak velocity amplitude in **c**, baseline 317/4, reserpine + L-DOPA 557/4. **f**–**j**, Individual (event heatmaps, top) and average (bottom) time courses of velocity amplitudes (**f**), and of $GRAB_{DA}$ (**g**) and tdTomato (**h**) fluorescence during contralateral movement initiations (left turns, velocity angles between 0° and 180°), and peak velocity (**i**) and $GRAB_{DA}$ (**j**) per mouse, for the experiment shown in Fig. 3k–n, RIM control data are replotted from Fig. 2j,l. Event heatmaps in **f**–**h** were sorted by the peak velocity amplitude in **f**, baseline 385/4, reserpine + L-DOPA 362/4. The observations that L-DOPA restored movement in RIM cKO^{DA} mice to pre-reserpine levels (**f**, Fig. 3k–n), and that dopamine denervation followed by apomorphine-induction of rotations was unaffected (Extended Data Fig. 1ac,ad), indicate that there is no strong sensitization of dopamine receptors or dopamine-modulated circuits after RIM ablation. Data are mean ± SEM; * $p < 0.05$, assessed by two-sided Mann-Whitney rank-sum tests in **i**, **j**.

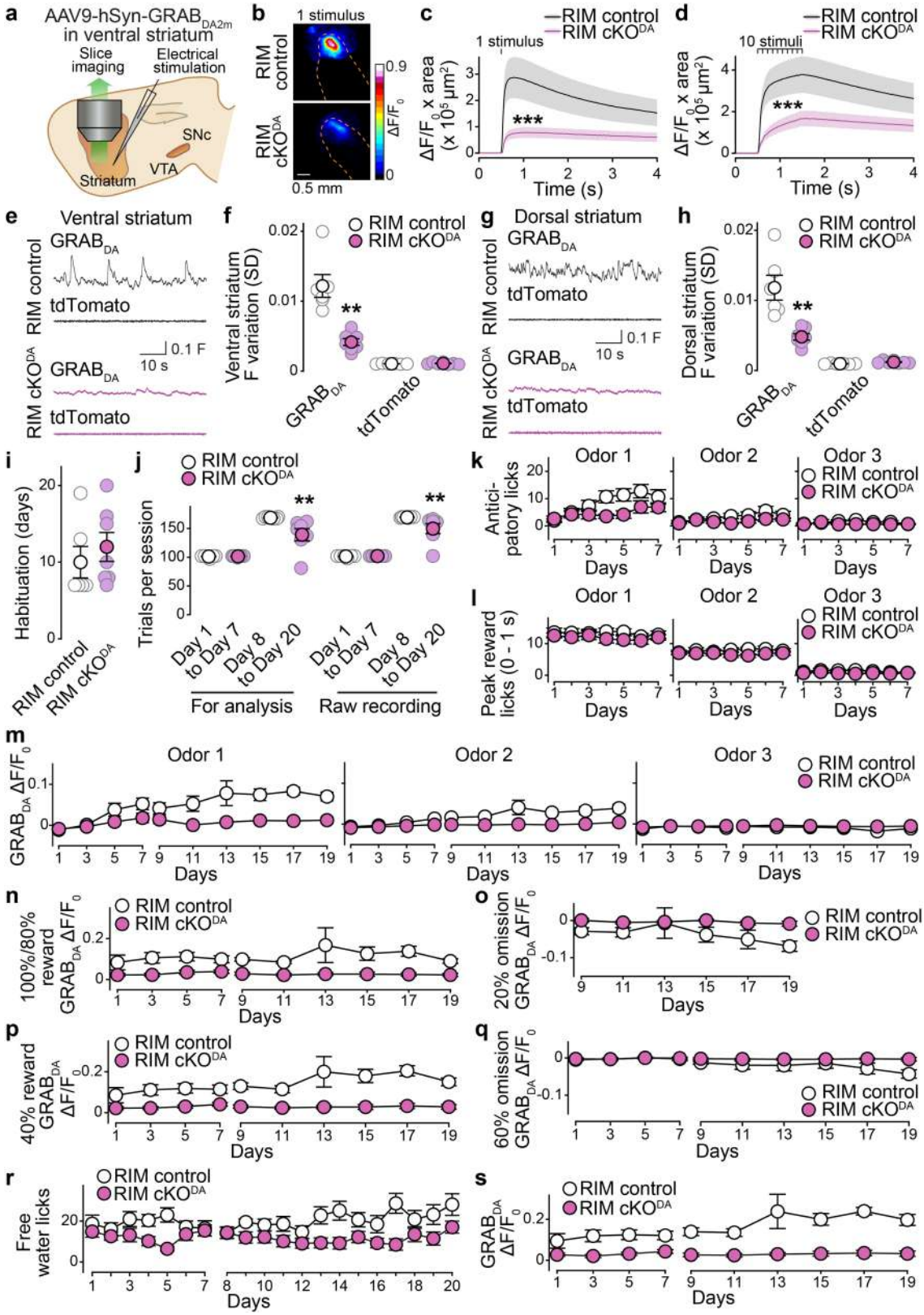

Extended Data Fig. 10 | See next page for caption.

Extended Data Fig. 10 | $GRAB_{DA}$ analyses in ventral striatum and additional analyses during the probabilistic cue-reward association task in RIM cKO^{DA} mice. a, Schematic of slice imaging. **b**–**d**, Representative images (**b**) and quantification (**c**,**d**) of dopamine release monitored by $GRAB_{DA}$ fluorescence in slices containing the ventral striatum (dashed lines outline the striatum), evoked by a single stimulus (**b**,**c**) or 10 stimuli (**d**, 10 Hz), RIM control 10 slices from 4 mice, RIM cKO^{DA} 10/4. **e**,**f**, Example traces (**e**) and quantification (**f**) of ventral striatum fluorescence variation quantified as standard deviation (SD) of $GRAB_{DA}$ and of tdTomato raw fluorescence on day 1 of the task in Fig. 5, RIM control 6 mice, RIM cKO^{DA} 7. **g**,**h**, As in **e** and **f**, but for dorsal striatum on day 2, n as in **e**,**f**. The in vivo deficits are overall similar in dorsal and ventral striatum. There might be an enhanced $GRAB_{DA}$ signal in ventral striatal brain slices compared to dorsal striatum (Fig. 1a–d) in RIM cKO^{DA} mice. This was not observed with amperometry[33], and could be because of differences in the roles of RIM, or technical differences in experiments, or because of detection of other transmitters by $GRAB_{DA}$, for example norepinephrine for which innervation is prominent in ventral but not dorsal striatum[31,47,48]. **i**, The number of habituation days for the experiment shown in Fig. 5, RIM control 6, RIM cKO^{DA} 7. **j**, Number of trials that the mice completed during each training phase. For analyses, only completed blocks were used, n as in **i**. **k**,**l**, Anticipatory licks (**k**) and peak licks to expected reward during the 1 s time window from water onset (**l**) for each odor during training days 1 to 7, n as in **i**. **m**, Average ventral striatum $GRAB_{DA}$ odour responses (within 3 s from odor onset), n as in **i**. **n**–**q**, Average ventral striatum $GRAB_{DA}$ reward responses (**n**, **p**, within 201 to 1200 ms from water onset) and reward omission responses (**o**, **q**, within 1501 to 2500 ms from water onset) for odours 1 (**n**,**o**) and 2 (**p**,**q**), n as in **i**. **r**,**s**, Total licks (**r**, within 1 to 3000 ms after water onset) and average $GRAB_{DA}$ fluorescence (**s**, within 201 to 1200 ms after water onset) for free water, n as in **i**. Data are mean ± SEM; ** $p < 0.01$, *** $p < 0.001$, assessed by two-sided Mann-Whitney rank-sum tests in **c**, **d**, **f**, **h**, **i**, **j**.

nature portfolio

Corresponding author(s): Pascal S. Kaeser

Last updated by author(s): Sep 27, 2024

Reporting Summary

Nature Portfolio wishes to improve the reproducibility of the work that we publish. This form provides structure for consistency and transparency in reporting. For further information on Nature Portfolio policies, see our Editorial Policies and the Editorial Policy Checklist.

Statistics

For all statistical analyses, confirm that the following items are present in the figure legend, table legend, main text, or Methods section.

n/a	Confirmed
☐	☒ The exact sample size (*n*) for each experimental group/condition, given as a discrete number and unit of measurement
☐	☒ A statement on whether measurements were taken from distinct samples or whether the same sample was measured repeatedly
☐	☒ The statistical test(s) used AND whether they are one- or two-sided *Only common tests should be described solely by name; describe more complex techniques in the Methods section.*
☒	☐ A description of all covariates tested
☐	☒ A description of any assumptions or corrections, such as tests of normality and adjustment for multiple comparisons
☐	☒ A full description of the statistical parameters including central tendency (e.g. means) or other basic estimates (e.g. regression coefficient) AND variation (e.g. standard deviation) or associated estimates of uncertainty (e.g. confidence intervals)
☐	☒ For null hypothesis testing, the test statistic (e.g. *F*, *t*, *r*) with confidence intervals, effect sizes, degrees of freedom and *P* value noted *Give P values as exact values whenever suitable.*
☒	☐ For Bayesian analysis, information on the choice of priors and Markov chain Monte Carlo settings
☒	☐ For hierarchical and complex designs, identification of the appropriate level for tests and full reporting of outcomes
☒	☐ Estimates of effect sizes (e.g. Cohen's *d*, Pearson's *r*), indicating how they were calculated

Our web collection on statistics for biologists contains articles on many of the points above.

Software and code

Policy information about availability of computer code

Data collection	Commercially available software was used for data collection (HCImage 4.2.6.1, Point Grey FlyCap2.13.3.61, Bonito CL-400B/C, ThorCam 3.6.0.6, MATLAB R2020b, Labview 2018) following previously described methodology (PMIDs: 35324301, 33147470, 14566341, 35798979) and as outlined in the methods section.
Data analysis	Commercially available software and open source software (MATLAB R2020b, DeepLabCut) were used for data analyses following procedures described before (PMIDs: 35324301, 30127430, 33147470, 35798979) and as outlined in the methods section; for statistics, GraphPad Prism 9.3.1 and MATLAB R2020b were used as described in the methods section.

For manuscripts utilizing custom algorithms or software that are central to the research but not yet described in published literature, software must be made available to editors and reviewers. We strongly encourage code deposition in a community repository (e.g. GitHub). See the Nature Portfolio guidelines for submitting code & software for further information.

Data

Policy information about availability of data

All manuscripts must include a data availability statement. This statement should provide the following information, where applicable:

- Accession codes, unique identifiers, or web links for publicly available datasets
- A description of any restrictions on data availability
- For clinical datasets or third party data, please ensure that the statement adheres to our policy

Data points generated for this study are included in the figures whenever possible. Tabulated data for all figures are available at https://zenodo.org/doi/10.5281/zenodo.13329864. Additional data are available from the corresponding author upon request. Reference data for stereotaxic injections are available at Allen Mouse Brain Atlas [mouse, P56, coronal]; atlas.brain-map.org (2011); reference 65.

Research involving human participants, their data, or biological material

Policy information about studies with human participants or human data. See also policy information about sex, gender (identity/presentation), and sexual orientation and race, ethnicity and racism.

Reporting on sex and gender	No human research participants.
Reporting on race, ethnicity, or other socially relevant groupings	No human research participants.
Population characteristics	No human research participants.
Recruitment	No human research participants.
Ethics oversight	No human research participants.

Note that full information on the approval of the study protocol must also be provided in the manuscript.

Field-specific reporting

Please select the one below that is the best fit for your research. If you are not sure, read the appropriate sections before making your selection.

☒ Life sciences ☐ Behavioural & social sciences ☐ Ecological, evolutionary & environmental sciences

For a reference copy of the document with all sections, see nature.com/documents/nr-reporting-summary-flat.pdf

Life sciences study design

All studies must disclose on these points even when the disclosure is negative.

Sample size	Sample sizes were determined based on previous studies and are similar to studies published in the field (PMIDs: 35324301, 37812725, 38093002, 35798979, 33345774).
Data exclusions	All data that met quality standards (described in the methods section) were included. No outliers were excluded for comparisons of genotypes or conditions.
Replication	The number of observations is reported in each figure. Data were acquired from multiple animals (mean: 6, range: 3 to 14).
Randomization	Data derived from animals were not randomized, but pooled by genotype and/or condition after analyses by a blinded experimenter were completed.
Blinding	For genotype comparisons, the experimenter was blind to genotype during data acquisition and analyses; for drug treatments, the experimenter was blind do the condition during data analyses. Data acquisition for drug treatments could not be blinded because the comparisons were made as pre- vs post-drug treatment, the treatment sequence was essential, and often only one drug was applied.

Reporting for specific materials, systems and methods

We require information from authors about some types of materials, experimental systems and methods used in many studies. Here, indicate whether each material, system or method listed is relevant to your study. If you are not sure if a list item applies to your research, read the appropriate section before selecting a response.

Materials & experimental systems

n/a	Involved in the study
☒	☐ Antibodies
☒	☐ Eukaryotic cell lines
☒	☐ Palaeontology and archaeology
☐	☒ Animals and other organisms
☒	☐ Clinical data
☒	☐ Dual use research of concern
☒	☐ Plants

Methods

n/a	Involved in the study
☒	☐ ChIP-seq
☒	☐ Flow cytometry
☒	☐ MRI-based neuroimaging

Animals and other research organisms

Policy information about studies involving animals; ARRIVE guidelines recommended for reporting animal research, and Sex and Gender in Research

Laboratory animals	Conditional RIM1 and RIM2 knockout mice (RIM1floxed, RRID:IMSR_JAX:015832, described in PMID: 19074017; RIM2floxed, RRID:IMSR_JAX:015833, described in PMID: 21241895), conditional Synaptotagmin-1 knockout mice (Syt-1floxed, RRID:IMSR_EM:06829, described in PMID: 26280336) and DATIRES-Cre mice (RRID:IMSR_JAX:006660, described in PMID: 16865686) were used. Intercrosses of these mice as used here were described before (RIM cKODA mice, PMIDs: 29398114 and 34767769; Syt-1 cKODA mice, PMID: 32490813). Surgeries were started at 30 days of age (80 ± 48 days; mean ± SD) and experiments were completed at 122 ± 67 days of age. Specifically, age ranges (mean ± SD) for completion of experiments were: 120 ± 71 days for Fig. 1a-d, Extended data figs. 1a-i and 10a-d), 135 ± 78 days for Fig. 1e-t and Extended data fig. 1j-af, 105 ± 50 days for Fig. 2 and Extended data figs. 2-5, 92 ± 54 days for Fig. 3 and Extended data figs. 6-9, 103 ± 11 days for Fig. 4, and 203 ± 21 days for Fig. 5 and Extended data fig. 10e-s. Mice used in behavioral experiments were housed in a reversed 12 h light-dark cycle in rooms set to 21 to 24 °C and 50% humidity, and behavioral experiments were conducted during the dark phase of the cycle.
Wild animals	The study did not include wild animals.
Reporting on sex	Female and male mice were included in all experiments irrespective of sex.
Field-collected samples	The study did not involve samples collected from the field.
Ethics oversight	Animal experiments were performed in accordance with approved protocols of the Harvard University Animal Care and Use Committee.

Note that full information on the approval of the study protocol must also be provided in the manuscript.

Plants

Seed stocks	No plants were used.
Novel plant genotypes	No plants were used.
Authentication	No plants were used.